Petrogenesis and 40Ar/39Ar dating of hydrothermal romanechite from the sub-aerial fault-related Romanèche Mn deposit (France)

Augustin Dekoninck, Gilles Ruffet, Julien Baptiste, Robert Wyns, Simon Philippo, Yishen Zhang, Olivier Namur

Journal Pre-proof

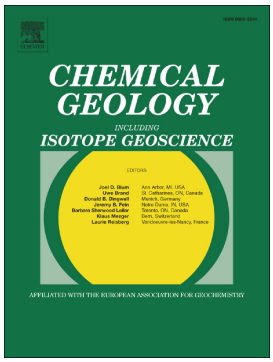

Petrogenesis and 40Ar/39Ar dating of hydrothermal romanechite from the sub-aerial fault-related Romanèche Mn deposit (France)

Augustin Dekoninck, Gilles Ruffet, Julien Baptiste, Robert Wyns, Simon Philippo, Yishen Zhang, Olivier Namur

PII: S0009-2541(22)00574-5

DOI: https://doi.org/10.1016/j.chemgeo.2022.121280

Reference: CHEMGE 121280

To appear in: *Chemical Geology*

Received date: 10 August 2022

Revised date: 29 November 2022

Accepted date: 21 December 2022

Please cite this article as: A. Dekoninck, G. Ruffet, J. Baptiste, et al., Petrogenesis and 40Ar/39Ar dating of hydrothermal romanechite from the sub-aerial fault-related Romanèche Mn deposit (France), *Chemical Geology* (2022), https://doi.org/10.1016/j.chemgeo.2022.121280

Petrogenesis and $^{40}Ar/^{39}Ar$ dating of hydrothermal romanechite from the sub-aerial fault-related Romanèche Mn deposit (France).

Augustin DEKONINCK[1,@], Gilles RUFFET[2,3], Julien BAPTISTE[4], Robert WYNS[4], Simon PHILIPPO[5], Yishen ZHANG[6], Olivier NAMUR[6]

[1]Institute of Life-Earth-Environment (ILEE), University of Namur, 61 rue de Bruxelles B-5000, Namur, Belgium. augustin.dekoninck@unamur.be

[2]CNRS (CNRS/INSU) UMR 6118, Géosciences Rennes, F-35042 Rennes Cedex, France. gilles.ruffet@univ-rennes1.fr

[3]Université de Rennes 1, Géosciences Rennes, 35042 Rennes, France. gilles.ruffet@univ-rennes1.fr

[4]BRGM (French Geological Survey), DGR/GAT, 1, Av. Cl. Guillemin, BP 36009, 45060 Orléans Cedex 2, France. j.baptiste@brgm.fr, r.wyns@free.fr

[5]Laboratoire de Minéralogie, Musée National d'Histoire Naturelle, Rue Münster 25, 2160 Luxembourg, Luxembourg. simon.philippo@mnhn.lu

Department of Earth and Environmental Sciences, KU Leuven, Celestijnlaan 200e – Box 2408, B-3001, Leuven, Belgium. yishen.zhang@kuleuven.be, olivier.namur@kuleuven.be

Abstract

This study discusses the hydrothermal formation of romanechite ($Ba_{0.7}Mn_{4.5}O_{10.}1.1H_2O$) in the Romanèche Mn deposit and the significance of its age by combining ore petrogenesis and $^{40}Ar/^{39}Ar$ ages. Romanechite occurs as a minor phase in various manganese deposit types and remains poorly studied in comparison with other K-bearing Mn oxides (i.e., coronadite group) because of its scarcity, small grain size, intermixing and poor crystallinity. The fault-controlled Romanèche Mn deposit (Massif Central, Eastern France) investigated herein exhibits a well-crystallized and late stage massive romanechite ore occurring in a quartz-barite-fluorite gangue. Petrographical and geochemical data support manganese ore formation under sub-aerial conditions with temperatures close to fluorite precipitation (100-200°C) and characterized by a Mn-Ba-W-As association. Five out of the eight studied samples have produced $^{40}Ar/^{39}Ar$ plateau ages ranging from 25.2±0.3 to 18.2±0.5 Ma. Despite a low K content (0.1-0.6 wt.% K), the good crystallinity of romanechite due to its epithermal formation likely favours a better production and/or retention of the radiogenic argon than poorly crystallized phases of supergene origin. Therefore, the dataset identifies a period of at least c. 7.6 My of discontinuous hydrothermal activity, which is consistent with graben-related fault reactivation and likely volcanic activity in the Massif Central. Ultimately, this study confirms the feasibility of romanechite $^{40}Ar/^{39}Ar$ dating.

Keywords: romanechite, manganese, $^{40}Ar/^{39}Ar$ dating, epithermal mineralization, Mn oxide

1. Introduction

Assessing the age of mineral deposition is a key issue to understand the timescales of formation of mineral resources. When datable minerals are present, it is of great importance to identify the process by which they have precipitated in order to better constrain the ore genesis. Mn oxides have long been used to date supergene deposits due to the extensive occurrence of K-bearing Mn oxides (e.g., Ruffet et al., 1996; Li et al., 2007; Beauvais and Chardon, 2013; Vasconcelos et al., 2013; Deng et al., 2016; Vasconcelos and Carmo, 2018; Jean et al., 2019; Dekoninck et al., 2019, 2021; De Putter and Ruffet, 2020). The most common species belong to the coronadite group [$(Ba^{2+},Pb^{2+},Sr^{2+},Na^{+},K^{+},)(Mn^{4+}Mn^{3+}$ or $^{2+})_8O_{16}$] (Lippolt and Hautmann, 1995; Ruffet et al., 1996; Vasconcelos et al., 1995, 1994, 1992) forming a typical tunnel. The tunnel Mn oxides are built of chains of edge-sharing MnO_6 octahedra, and the chains share corners to produce frameworks that have tunnels with square or rectangular cross sections (Post, 1999). The 2X2 tunnel crystallographic structure of coronadite allows a good retentivity of the $^{40}Ar^*$ produced by the decay of radioactive structural ^{40}K, hence providing a remarkable tool for $^{40}Ar/^{39}Ar$ dating. Far less known, romanechite $[Ba_{0.66}Mn^{4+}_{3.68}Mn^{3+}_{1.32}O_{10}.1.34.H_2O]$ or $(Ba,H_2O)_2(Mn^{3+},Mn^{4+})_5O_{10}$ (Post, 1999; Turner and Post, 1988) is also suitable for $^{40}Ar/^{39}Ar$ geochronology (Vasconcelos, 1999) as it can host structural K in the 2X3 tunnel structure (Burns and Burns, 1979; Post, 1999).

Although the majority of Mn oxides precipitate under supergene conditions, many deposits host Mn oxides directly formed from hydrothermal solutions (Choubert and Faure-Muret, 1973; Conly et al., 2011; Decrée et al., 2010; Dekoninck et al., 2018; Glasby et al., 2005; Hewett, 1964; Leal et al., 2008; Liakopoulos et al., 2001; O'Reilly, 1992; Papavassiliou et al., 2017; Roy, 1981, 1968). The Mn oxide ore precipitates on top of the hydrothermal system by mixing of ascending hydrothermal fluids with descending oxygenated meteoric water (Hewett, 1964; Roy, 1968, 1981). These sub-surface hypogene ores are composed of higher valence oxides such as romanechite, coronadite group minerals, pyrolusite and ramsdellite. Whereas discriminating between Mn oxides formed under supergene versus epithermal conditions is relatively simple in active systems, it remains challenging in ancient ore systems (i.e. Gossans).

The Romanèche manganese deposit (Saône-et-Loire department, France)(Fig. 1) is predominantly composed of romanechite (type-locality mineral; Lacroix, 1910) located atop

a vein-type mineralization (Fig. 2; Bouladon, 1958). The Mn oxide ore is trapped in and aside the boundary fault-zone separating the Massif Central (MC) Variscan granitic basement and the Bresse graben filled by Mesozoic and Cenozoic sediments (Figs. 1 and 2). The mineralization has long been considered as a supergene gossan capping an underlying and hidden hydrothermal mineralization (Dolomieu, 1796; Drouot, 1857; Hautmann and Lippolt, 2000; Lacroix, 1910; Lougnon, 1981) due to the predominance of tetravalent Mn oxides. However, Bouladon (1958) was the first to argue for an hydrothermal formation of the romanechite stage. Therefore, the Romanèche deposit can be useful to discuss the hydrothermal versus supergene formation of Mn oxides on top of vein-type mineralization.

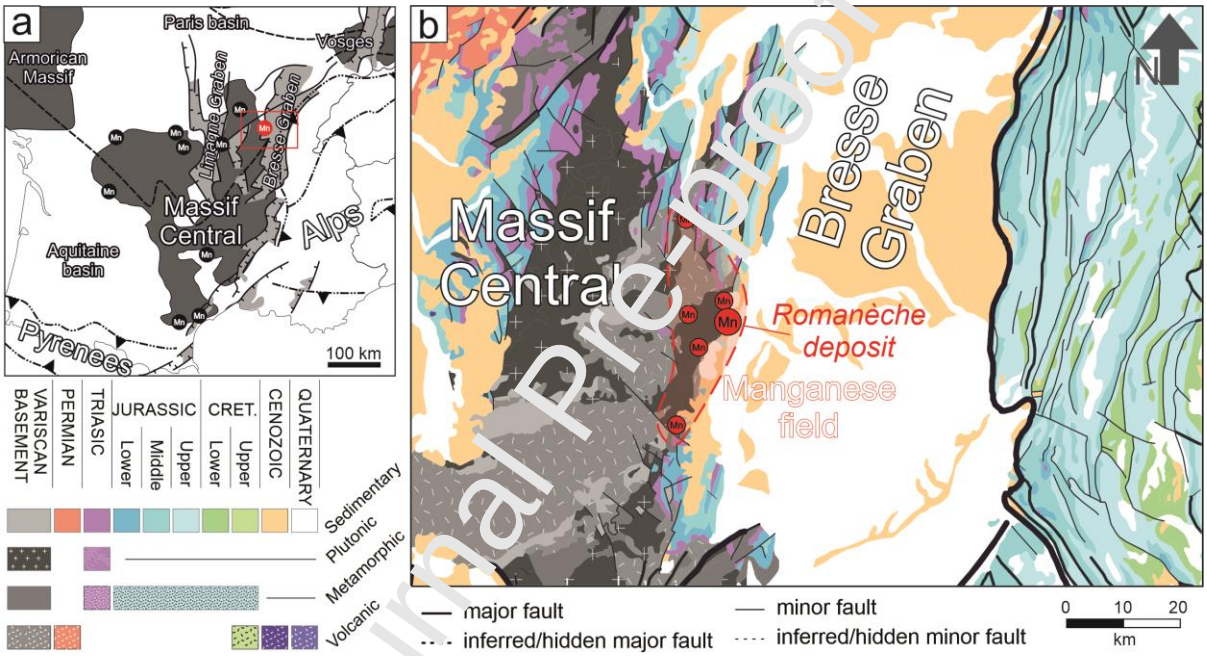

Fig. 1. Geological situation of the Romanèche Mn deposit and surrounding Mn mineralization. **a.** Location of the Romanèche deposit among other Mn occurrences of the French Massif Central. **b.** Geological map of the Romanèche Mn(-F) manganese field between the Massif Central and the Bresse Graben (modified after Chantraine et al., 2003).

Hautmann and Lippolt (2000) were the first, as part of a global Central European study of Mn-oxides, to conduct a geochronological analysis of this deposit in order to discuss weathering processes in Western Europe. Our study provides a more detailed analysis of the composition, ore genesis and timing of the Romanèche manganese deposit by combining X-ray diffraction (XRD), scanning electron microscope with energy-dispersive spectroscopy (SEM-EDX), electron probe micro-analysis (EPMA), whole rock geochemistry and $^{40}Ar/^{39}Ar$ dating of romanechite. This dataset is used to refine the formation process of romanechite and

to provide new ages in order to better understand the formation of the Romanèche deposits and other similar deposits worldwide.

2. Hydrothermal Mn oxide deposits

Hydrothermal Mn deposits are known worldwide. They all have low tonnage and reserves (e.g., Ouarzazate Mn field, Morocco; Cape Vani, Greece; SW, USA; Choubert and Faure-Muret, 1973; Conly et al., 2011; Decrée et al., 2010; Dekoninck et al., 2018; Glasby et al., 2005; Hewett, 1964; Holtstam and Mansfeld, 2001; Leal et al., 2008; Liakopoulos et al., 2001; O'Reilly, 1992; Papavassiliou et al., 2017; Roy, 1981, 1968). These deposits are fault-controlled and occur as veins that may be up to 1.5 m thick, extend horizontally up to 500 m and be traced to depths of up to 150 m. The vertical extension is rarely beyond 1 km (Hewett, 1964). The Mn oxide ore precipitates in the upper part of the hydrothermal system, showing an increasing gradation of higher valence oxides, including the Mn^{4+}-Mn^{3+}-bearing romanechite, coronadite group minerals, pyrolusite and ramsdellite (Hewett, 1964; Roy, 1981, 1968). They show high concentrations of Ba, As, W, Sr, Be, Sb, Tl and Ge. They are consistently accompanied by barite, fluorite, quartz and carbonates as gangue minerals. Silicification is the most common form of wall-rock alteration near the main Mn vein (Hewett, 1964). Sericitization is also reported. Barite and fluorite precipitation can either predate or postdate the Mn oxides. Argentosiderite is found in some places and is a proof of hydrothermalism (Hewett, 1964). Below the high-valence Mn oxide ore, the deeper ore includes Mn^{2+}-bearing minerals such as carbonates, silicate and oxides (Fusswinkel et al., 2013; Hewett, 1966; Madondo et al., 2020).

3. Mineralization style

The Romanèche manganese deposit is associated to the major fault-zone separating the Variscan granitic basement of the MC and the Triassic-Jurassic cover of the Bresse Graben. The Mn ore follows this structure over an NNE striking length of c. 750 m (Figs. 1b and 2). This fault has an offset of ~650 meters and has been active several times since the Variscan orogenesis (Bouladon, 1958). The Romanèche deposit is no longer accessible; the numerous galleries have been closed by the regional authorities. The main access has been sealed by a concrete cap behind the Romanèche church and the other wells obstructed since the eighties. Therefore, the today's Mn ore consists of mining wastes reused in some walls of the village or disseminated in the surrounding vineyards (see Appendix A). The only direct observations of the ore are minor Mn veins hosted in granites. Several Mn occurrences outcrop over a

greater area with fluorite and barite (Drouot, 1857), which defines a larger manganiferous field of 10x35 km² following the major fault direction (Fig. 1b). The Mn deposit consists of (i) two parallel lodes ("Grand filon" and "Petit filon") with a N35°E direction and dip angles of 50-75°SE hosted in Carboniferous granites ("Petit filon") or in the fault zone ("Grand filon") and (ii) a stratabound epigenetic mineralization replacing the Sinemurian limestone (Fig. 2; Lacroix, 1910; Bouladon, 1958). Both mineralization styles are reworked in the alluvium cover. The Romanèche ore combines romanechite with fluorite, quartz and barite. Three major ore facies can be observed: (1) Mn crust (Fig. 3a), (2) Massive Mn ore (with or without fluorite; Fig. 3b), (3) Mn breccia (Fig. 3c). Hematite is also present in little amounts but becomes abundant at depth with barite (Bouladon, 1958; Lacroix, 1910) and locally arseniosiderite $Ca_2Fe_3O_2(AsO_4)_3.3H_2O$ (type-locality mineral, Dufrénoy, 1842).

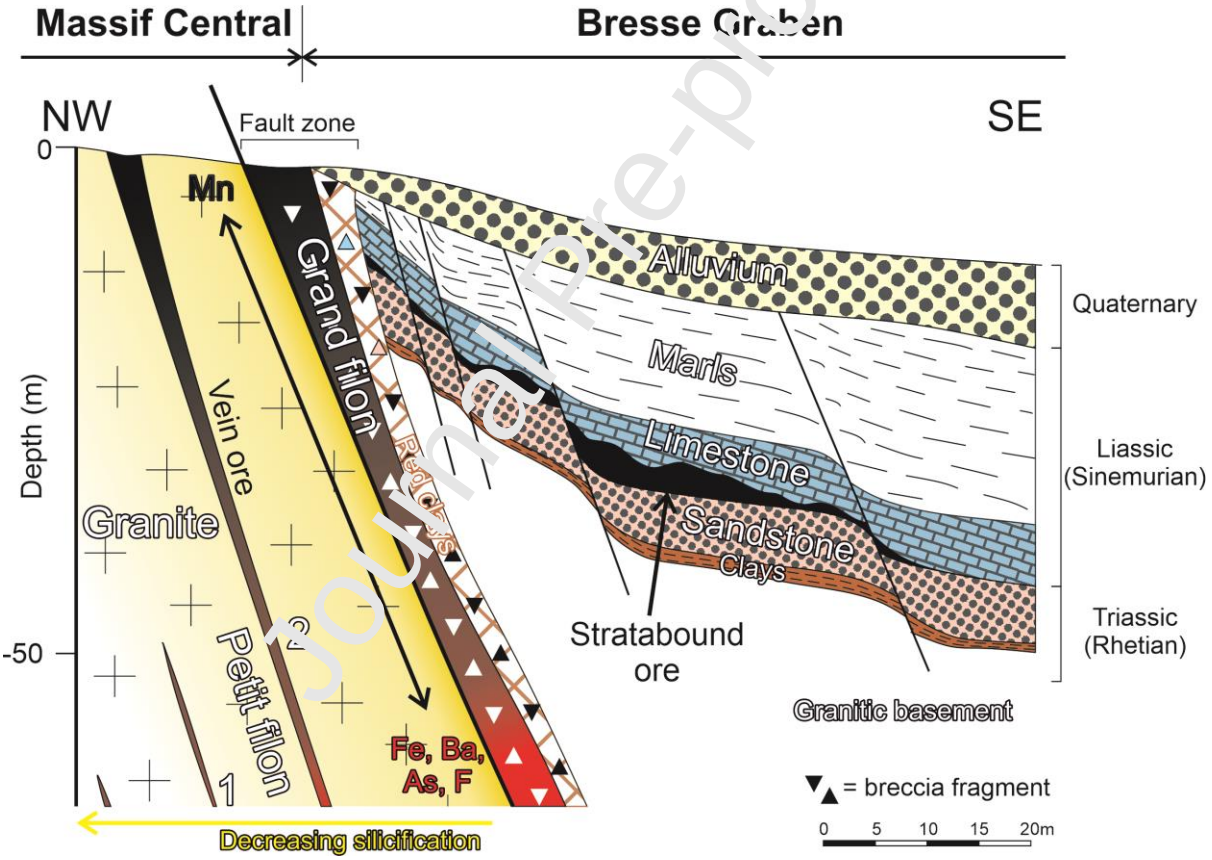

Fig. 2. N125°E cross-section through the Romanèche deposit (Bouladon, 1958).

4. Materials and methods

Forty-four samples have been collected in the field. Most of them come from mining wastes in vineyards and village walls around the main historical mining wells (see Appendix A for details and photographs). One sample is from the collection of the Museum National d'Histoires Naturelles du Luxembourg. The initial location of these samples is unknown but

they likely come from the most important past extraction sites. The mineralogy of 32 samples of these samples was determined by X-ray diffraction. Sixteen samples were further selected and examined in detail by optical and scanning electron microscopy on polished sections. EPMA analyses has been carried on romanechite to obtain quantitative chemical analyses of major and minor elements. This mineralogical and petrographical determination was complemented by geochemical analyses of major and trace elements on 14 whole rock samples. Based on these results, we selected eight samples for $^{40}Ar/^{39}Ar$ geochronology.

4.1 Mineralogical and petrographical analysis

Polished sections (16) were prepared for petrographic analyses at the Geomaterial Preparation Laboratory of the University of Namur (Belgium). XRD analyses of powdered samples were performed using an X-ray Panalytical X'Pert Pro diffractometer and a PHILLIPS PW3710 (CuKα radiation) of the PC2 platform (University of Namur), operating at 40 kV and 30 mA. The main mineral phases were identified using the ICDD View software with PDF-2 database (Powder Diffraction File 2019). Polished sections were studied by optical microscopy and electron microscopy using a JEOL 6010 LV and a JSM 7500-F SEM coupled with an ULTRA MINI-CUP Energy Dispersive Spectrometer (EDS) hosted at the Microscopy Service of the University of Namur. Four polished sections have also been observed and analyzed with a JEOL JXA-8530F EPMA equipped with a high brightness Schottky field emission electron gun (FEG), at the Department of Materials Engineering of KU Leuven (Leuven, Belgium). The following primary standards were used for Kα calibration: Mn metal (Mn), quartz (Si), almandine garnet (Al), barite (Ba), skutterudite (As, Co), hematite (Fe), plagioclase-An65 (Na), biotite (Mg), anhydrite (Ca), galena (Pb), celestite (Sr), sphalerite (Zn), tungsten metal (WO_3) and cuprite (Cu). Details about standards, accuracy, precision and analytical conditions are given in Appendix A – Supplementary Material. The water content is calculated using charge base structural formulae (Table 1).

Table 1. EPMA analysis of romanechite in the Romanèche Mn deposit.

Label	No.	SiO_2	Al_2O_3	BaO	MnO_2	As_2O_5	FeO	Na_2O	MgO	CaO	K_2O	PbO	SrO	ZnO	WO_3	CuO	CoO	H_2O^*	Total
19ROM	0	0.1	0.51	16.	75.	0.45	0.0	0.02	0.05	0.1	0.0	0.0	0.2	0.0	2.10	0.0	0.0	4.8	100.

15		4		45	53		9			3	3	0	4	1		5	4	4	67
19ROM15	1	0.03	0.46	16.67	75.38	0.30	0.08	0.08	0.00	0.15	0.02	0.01	0.16	0.00	2.61	0.20	0.04	4.78	100.98
19ROM15	6	0.08	0.43	15.62	75.15	0.33	0.13	0.31	0.00	0.22	0.05	0.00	0.20	0.00	3.01	0.05	0.00	4.71	100.30
19ROM15	7	0.00	0.41	15.72	75.07	0.68	0.09	0.11	0.03	0.18	0.03	0.00	0.34	0.02	2.23	0.08	0.02	4.79	99.80
19ROM15	8	0.00	0.45	16.50	75.12	0.13	0.03	0.02	0.06	0.15	0.02	0.01	0.29	0.00	2.06	0.03	0.07	4.74	99.67
19ROM15	9	0.03	0.51	16.21	74.98	0.65	0.09	0.02	0.03	0.13	0.05	0.00	0.26	0.00	1.99	0.05	0.06	4.81	99.86
19ROM15	10	0.00	0.47	16.82	75.80	0.46	0.11	0.03	0.03	0.08	0.01	0.00	0.20	0.00	1.74	0.00	0.09	4.81	100.65
19ROM15	11	0.08	0.51	16.73	77.16	0.34	0.05	0.07	0.01	0.12	0.01	0.00	0.20	0.00	2.18	0.05	0.04	4.92	102.48
19ROM15	12	0.16	0.51	16.5	77.5	0.09	0.07	0.05	0.02	0.08	0.02	0.00	0.14	0.00	2.40	0.04	0.00	4.99	102.72

				7	8													
19ROM15	13	0.08	0.44	16.10	76.93	0.36	0.10	0.09	0.00	0.13	0.02	0.00	0.17	0.00	2.32	0.04	0.01	4.95	101.72
19ROM15	14	0.01	0.48	16.37	75.80	0.56	0.12	0.03	0.04	0.15	0.03	0.00	0.27	0.00	2.05	0.07	0.06	4.85	100.87
19ROM15	15	0.00	0.47	16.38	76.16	0.47	0.06	0.09	0.00	0.10	0.03	0.00	0.32	0.00	2.06	0.07	0.01	4.83	101.05
19ROM15	5	0.03	0.53	16.58	76.27	0.06	0.50	0.05	0.08	0.13	0.02	0.01	0.12	0.00	2.12	0.10	0.04	4.89	101.53
19ROM15	4	0.00	0.53	16.34	74.92	0.09	0.08	0.08	0.00	0.14	0.02	0.06	0.15	0.00	1.93	0.12	0.00	4.76	99.72
19ROM15	3	0.05	0.48	16.43	77.03	0.21	1.00	0.18	0.02	0.19	0.06	0.08	0.15	0.00	1.97	0.11	0.05	4.88	102.90
19ROM15	2	0.00	0.29	16.27	75.11	0.03	1.25	0.02	0.00	0.14	0.04	0.13	0.16	0.00	1.73	0.09	0.09	4.83	100.16
19ROM32a	16	0.01	0.49	16.93	73.27	0.06	0.55	0.01	0.00	1.48	0.25	0.00	1.00	0.00	0.96	0.01	0.01	4.01	99.04

19ROM32a	17	0.00	0.47	16.26	77.62	0.32	0.37	0.20	0.00	1.15	0.11	0.00	0.35	0.02	0.77	0.02	0.01	4.54	102.22
19ROM32a	18	0.07	0.54	16.31	78.50	0.20	0.32	0.13	0.07	1.05	0.12	0.00	0.24	0.02	0.76	0.03	0.01	4.70	103.06
19ROM32a	19	0.01	0.48	16.25	73.07	0.20	0.45	0.14	0.07	1.04	0.16	0.00	0.61	0.03	0.86	0.02	0.00	4.18	97.56
19ROM32a	20	0.00	0.40	14.80	77.07	0.74	0.16	0.11	0.02	0.48	0.21	0.00	0.47	0.02	1.19	0.00	0.01	4.84	100.52
19ROM32a	21	0.00	0.40	14.50	78.92	0.80	0.13	0.16	0.03	0.40	0.18	0.00	0.61	0.00	0.80	0.01	0.00	4.98	101.88
19ROM32a	22	0.09	0.40	14.21	78.86	0.66	0.12	0.17	0.00	0.43	0.25	0.00	0.74	0.03	0.45	0.04	0.01	4.94	101.39
19ROM32a	23	0.04	0.47	15.89	77.71	0.26	0.45	0.11	0.10	1.07	0.18	0.00	0.37	0.01	1.03	0.03	0.01	4.65	102.39
19ROM32a	24	0.00	0.41	13.16	77.72	0.86	0.12	0.24	0.02	0.62	0.32	0.00	0.66	0.01	0.45	0.02	0.03	4.85	99.48
19R	25	0.	0.	1	7	0.	0.	0.	0.	0.	0.	0.	0.	0.	0.	0.	0.	4.	99

OM 32a		29	42	4.47	6.33	55	52	31	01	92	26	03	68	00	04	04	01	53	.40
19ROM 32a	26	0.00	0.45	16.37	78.70	0.66	0.11	0.10	0.00	0.25	0.06	0.00	0.30	0.00	0.00	0.00	0.04	4.91	101.94
19ROM 32a	27	0.12	0.47	16.95	79.69	0.41	0.10	0.00	0.02	0.07	0.05	0.00	0.17	0.04	0.13	0.00	0.00	5.06	103.28
19ROM 32a	28	0.00	0.47	15.75	76.66	1.02	0.07	0.18	0.00	0.51	0.07	0.00	0.29	0.03	0.11	0.03	0.02	4.72	99.92
19ROM 32a	34	0.00	0.51	16.82	78.88	0.21	0.23	0.12	0.10	0.55	0.07	0.00	0.19	0.01	0.58	0.00	0.02	4.81	103.09
19ROM 32a	35	0.03	0.47	16.90	80.08	0.28	0.33	0.17	0.07	0.74	0.10	0.00	0.18	0.01	0.69	0.00	0.00	4.83	104.88
19ROM 32a	36	0.38	0.50	16.24	76.81	0.56	0.36	0.14	0.00	0.35	0.10	0.04	0.14	0.00	1.13	0.00	0.00	4.84	101.60
19ROM 32a	42	0.12	0.40	13.69	78.37	0.75	0.09	0.23	0.03	0.64	0.31	0.00	0.63	0.03	0.51	0.01	0.02	4.86	100.71
	max	0.3	0.54	16.	80.	1.02	1.2	0.31	0.10	1.4	0.3	0.1	1.0	0.0	3.01	0.2	0.0	5.0	104.

		8		95	08		5			8	2	3	0	4		0	9	6	88
	min	0.00	0.29	13.16	73.07	0.00	0.03	0.00	0.00	0.07	0.01	0.00	0.12	0.00	0.00	0.00	0.00	4.01	97.56
	average	0.06	0.46	15.98	76.74	0.41	0.27	0.11	0.03	0.42	0.10	0.01	0.3	0.01	1.36	0.04	0.02	4.78	100.92

4.2 Whole rock geochemistry

Whole rock geochemical analyses were performed at the Activation Laboratories Ltd (Canada) for major and trace elements (Table 2). Sample powders were prepared using a RETSCH PM 100 planetary ball mills (University of Namur). REE and trace elements were analysed by lithium metaborate/tetraborate fusion Mass Spectrometry (FUS-MS) and major elements by Fusion Inductively Coupled Plasma Optical Emission Spectrometry (FUS-ICP). FeO was quantified by titration. Trace elements Ba, Sc, Be, Sr, Y, Zr and V were determined with FUS-ICP. FUS-ICP and ICP-OES was used to measure Pb and Mo concentrations, after a 4-acid digestion (hydrochloric-nitric perchloric-hydrofluoric), when values were higher than the detection limits (10,000 ppm and 100 ppm, respectively). In addition, sulfate (SO_4) was determined by infrared (IR) spectrometry and fluor (F) by lithium borate fusion with ion selective electrode. Fe_2O_3t is the measured total amount of iron enclosing Fe_2O_3 and FeO.

Table 2. Major oxides (in wt. %) and trace element (in ppm) geochemical analyses. LOI: Lost on ignition. Mineral abbreviation: ca=calcite, ro=romanechite, q=quartz, he=hematite, ba=barite, f=fluorite, ho=hollandite.

Analyte Symbo	Unit	D.L.	Analysis Metho	19ROM12	19ROM17	19ROM43	19ROM09	19ROM15	19rom20c	19rom21a	19rom21e	19ROM26	19ROM29	19rom32a	19rom32b	19ROM33	19ROM37
							Ca, Ro	Ro, Q	Ro, Q	Ro,	Qz,	F, Ba,	F, Q,	F, Ro	Q, F,	Ro,	F, Ro

l			d				, Q			He, Q	Ro	Q, Ro	Ro	, Ho	Ro	Q, F	, Ho
				Granite (wt.)	Gneiss	Granite	Mn ore	Mn ore	Mn ore	Mn-Fe ore	Mn ore	Mn ore	Mn ore	Mn ore	Mn-Fe ore	Mn ore	Mn ore
F	%	0.01	FUS-ISE	0.03	0.01	<0.01	0.74	0.01	0.03	0.15	0.07	14.[illegible]	34.6	16.4	6.41	2.73	42.2
SO_4	%	0.05	SO4	<0.05	<0.05	<0.05	<0.05	<0.05	0.[illegible]	<0.05	0.06	18.4	0.41	0.05	0.09	0.5	<0.05
SiO_2	%	0.01	FUS-ICP	69.92	74.19	71.[illegible]06	3.4	6	2.59	11.28	89.1	24.94	5.73	0.4	38.85	3.92	0.64
Al_2O_3	%	0.01	FUS-ICP	14.28	14.63	13.39	0.87	1.48	1.68	1.02	1.67	0.59	0.11	0.14	0.34	1.48	0.16
Fe_2O_3	%	0.01	FUS-ICP	1.89	0.81	0.26	0.97	0.41	0.79	15.96	0.63	<0.01	1.48	0.38	12.83	0.8	0.33
Mn	%	0	FU	0.035	0.015	0.019	46.03	56.59	58.9	43.34	5.116	0.028	12.24	43.09	17.61	54.79	7.418

O			S-ICP														
MgO	%	0.01	FUS-ICP	0.95	0.54	0.56	0.21	0.14	0.11	0.06	0.03	0.04	0.02	0.02	0.04	0.13	0.02
CaO	%	0.01	FUS-ICP	0.67	0.51	0.25	12.47	0.2	0.41	0.67	0.25	24.17	52.84	25.6	10.03	4.83	63.58
Na_2O	%	0.01	FUS-ICP	2.39	4.7	0.66	0.1	0.26	0.04	0.07	0.06	0.01	0.02	0.04	0.04	0.05	0.02
K_2O	%	0.01	FUS-ICP	5.75	2.12	9.96	0.47	0.33	0.34	0.69	1.04	0.22	0.05	0.99	0.15	0.4	0.06
TiO_2	%	0	FUS-ICP	0.417	0.2212	0.219	0.0043	0.0037	0.0039	0.0032	0.0021	0.0018	0.0003	0.0003	0.001	0.0044	0.0005
P_2O_5	%	0.01	FUS-ICP	0.25	0.21	0.16	0.08	0.02	0.16	0.04	0.03	0.05	0.04	0.03	0.02	0.03	< 0.01

LOI	%		GRAV	2.69	1.47	0.89	17.35	10.14	11.06	9.1	1.21	6.31	5.81	7.92	8.32	11.79	2.41
LOI2	%		FUS-ICP	2.75	1.56	1.05	17.36	10.14	11.06	9.11	1.21	6.33	5.81	7.92	8.32	11.79	2.41
Total	%	0.01	FUS-ICP	99.83	100.2	98.83	82.01	75.62	76.11	82.28	99.16	56.51	78.35	78.62	88.25	78.3	74.65
Total2	%	0.01	FUS-ICP	99.89	100.3	98.99	82.0[illegible]	75.62	76.11	82.28	99.16	56.5	78.36	78.62	88.25	78.3	74.65
Fe_2O_3(T)	%	0.01	FUS-ICP	2.55	1.69	1.82	0.98	0.43	0.8	15.97	0.64	0.18	1.49	0.39	12.84	0.82	0.34

Table 2. Continued.

Analyte Symbo	Unit	D.L.	Analysis Method	19ROM12	19ROM17	19ROM43	19ROM09	19ROM15	19rom20c	19rom21a	19rom21e	19ROM26	19ROM29	19rom32a	19rom32b	19ROM33	19ROM37
							Ca, Ro, Q	Ro, Q	Ro, Q	Ro, He	Qz, Ro	F, Ba, Q,	F, Q, Ro	F, Ro,	Q, F, Ro	Ro, Q,	F, Ro,

l										, Q		Ro		Ho		F	Ho
				Granite (wt.)	Gneiss	Granite	Mn ore	Mn ore	Mn ore	Mn-Fe ore	Mn ore	Mn ore	Mn ore	Mn ore	Mn-Fe ore	Mn ore	Mn ore
Sc	ppm	1	FUS-ICP	6	11	3	3	7	3	2	< 1	1	1	1	< 1	2	2
Be	ppm	1	FUS-ICP	6	2	3	60	29	14	86	5	1	17	36	37	44	13
V	ppm	5	FUS-ICP	37	15	19	58	295	94	59	9	7	10	45	20	57	20
Cr	ppm	20	FUS-MS	150	140	180	20	20	50	70	300	70	40	20	180	< 20	< 20
Co	ppm	1	FUS-MS	7	2	2	50	390	59	22	6	< 1	4	25	18	49	< 1
Ni	pp	20	FU	< 20	< 20	< 20	70	20	40	< 20	< 20	< 20	< 20	< 20	< 20	40	< 20

	m		S-MS														
Cu	ppm	10	FUS-MS	20	10	20	10	640	130	140	20	< 10	50	70	30	80	40
Zn	ppm	30	FUS-MS	40	< 30	< 30	220	30	200	330	< 30	< 30	40	50	160	160	< 30
Ga	ppm	1	FUS-MS	29	23	23	15	35	21	38	16	1	6	19	24	30	4
Ge	ppm	1	FUS-MS	2	2	3	41	110	38	69	6	1	11	34	57	41	5
As	ppm	5	FUS-MS	43	48	17	3550	2520	2270	6760	264	16	1450	2040	3450	2090	894
Rb	ppm	2	FUS-MS	278	100	379	46	16	26	48	49	21	4	24	13	33	5

Sr	ppm	2	FUS-ICP	278	94	112	3337	2354	2412	2535	364	2904	684	2149	905	2822	479
Y	ppm	1	FUS-ICP	15	36	9	12	8	13	12	3	38	21	16	15	11	12
Zr	ppm	2	FUS-ICP	179	210	95	21	19	13	14	24	16	6	66	5	17	7
Nb	ppm	1	FUS-MS	13	5	5	< 1	< 1	< 1	< 1	< 1	2	1	< 1	< 1	< 1	< 1
Mo	ppm	2	FUS-MS	< 2	< 2	< 2	129	43	176	137	18	< 2	36	182	61	142	18
Ag	ppm	0.5	FUS-MS	0.5	0.5	< 0.5	< 0.5	< 0.5	< 0.5	0.5	1	2.7	< 0.5	< 0.5	< 0.5	< 0.5	< 0.5
In	ppm	0.2	FUS-	< 0.2	< 0.2	< 0.2	< 0.2	< 0.2	< 0.2	< 0.2	< 0.2	< 0.2	< 0.2	< 0.2	< 0.2	< 0.2	< 0.2

			MS														
Sn	ppm	1	FUS-MS	9	8	5	< 1	< 1	< 1	1	1	< 1	< 1	< 1	1	< 1	< 1
Sb	ppm	0.5	FUS-MS	1.7	1.7	1.4	11	119	38.7	168	10.4	4.5	30	34.7	94.6	35.5	37.4
Cs	ppm	0.5	FUS-MS	30	15.4	4.4	18.9	7.2	7.5	11.8	3.3	6.4	1.9	1	5.1	11.7	2.1
Ba	ppm	2	FUS-ICP	1218	527	691	95190	1436 00	1403 00	97380	10840	2483 00	33160	81260	39980	1303 00	15610
La	ppm	0.1	FUS-MS	23.2	22.2	12.5	21.2	27.8	9.8	24.8	4.1	5.2	15.7	13.9	14.4	12.4	9.5
Ce	ppm	0.1	FUS-MS	84.8	52.3	27	18.4	23.3	14.4	40.9	8.2	8	17.2	12.3	32.2	11	9.1
Pr	p	0	F	5.6	6.6	2.9	4.1	5.8	2.2	4.1	0.9	1.0	2.7	2.2	3	2.1	1.7

	pm	.05	US-MS	6	6	3		6	8	4	8	5	5	1		1	1
Nd	ppm	0.1	FUS-MS	21.5	28	10.4	16	23.4	10.4	14.1	3.8	4.8	10.1	8.6	10.6	9	6.4
Sm	ppm	0.1	FUS-MS	4.2	7.4	2.5	2.7	5.2	2.8	2.7	0.8	2.1	2.4	1.8	2.3	1.9	1.4
Eu	ppm	0.05	FUS-MS	0.89	1.04	0.59	< 0.05	< 0.05	< 0.05	0.87	0.13	< 0.05	0.82	< 0.05	0.92	< 0.05	0.27
Gd	ppm	0.1	FUS-MS	3.5	7.5	2.1	2.7	4	3.2	2.6	0.6	2.8	2.7	1.9	2.6	2.1	1.4
Tb	ppm	0.1	FUS-MS	0.6	1.2	0.3	0.4	0.5	0.4	0.4	0.1	0.5	0.4	0.3	0.4	0.3	0.2
Dy	ppm	0.1	FUS-M	3	7.1	1.9	2.1	2.2	2.2	2.2	0.5	3.3	2.3	1.7	2.2	1.6	1.3

			S													
Ho	ppm	0.1	FUS-MS	0.5	1.3	0.3	0.4	0.4	0.4	0.4	<0.1	0.7	0.4	0.3	0.4	0.3	0.3
Er	ppm	0.1	FUS-MS	1.5	3.2	0.9	1.2	0.9	1.2	1	0.3	1.7	1	0.8	1.1	0.9	0.6
Tm	ppm	0.05	FUS-MS	0.23	0.42	0.14	0.16	0.13	0.1	0.12	<0.05	0.21	0.12	0.1	0.12	0.12	0.08
Yb	ppm	0.1	FUS-MS	1.5	2.6	0.9	1.1	0.8	1	0.7	0.2	1.2	0.7	0.6	0.6	0.7	0.5
Lu	ppm	0.01	FUS-MS	0.21	0.39	0.14	0.14	0.12	0.13	0.08	0.02	0.15	0.09	0.09	0.09	0.1	0.07
Hf	ppm	0.2	FUS-MS	4.9	6.2	2.9	0.7	0.7	0.6	<0.2	0.5	0.6	0.3	1.6	<0.2	0.3	<0.2
Ta	pp	0.	FU	1.7	0.6	1.3	0.2	0.1	0.3	0.3	<0.1	0.7	0.5	0.5	0.1	0.3	0.6

	m	1	S-MS														
W	ppm	1	FUS-MS	19	15	20	1710	13200	3140	2010	150	5	839	1670	1000	2410	1030
Tl	ppm	0.1	FUS-MS	3.3	1.2	2	269	30.1	105	57.7	48	0.1	22.4	172	32.8	75.1	21.9
Pb	ppm	5	FUS-MS	29	8	34	8	107	21	569	17	30	91	34	380	30	117
Bi	ppm	0.4	FUS-MS	< 0.4	< 0.4	< 0.4	< 0.4	11.6	< 0.4	< 0.4	< 0.4	< 0.4	< 0.4	< 0.4	< 0.4	< 0.4	< 0.4
Th	ppm	0.1	FUS-MS	21.5	8.5	15.2	1.1	0.4	1.5	2.1	1.5	1.6	0.2	0.1	0.5	1.3	0.3
U	ppm	0.1	FUS-MS	5.2	1.9	4.2	21.8	3.4	35.1	36.2	5.7	1.3	23.2	49.8	20.9	56.1	14.9

Fe O	%	0.1	TIR	0.6	0.8	1.4	< 0.1	< 0.1	< 0.1	< 0.1	< 0.1	0.2	< 0.1	< 0.1	< 0.1	< 0.1	< 0.1

4.3 $^{40}Ar/^{39}Ar$ K-Mn oxides geochronology

The eight romanechite sub-samples selected for geochronology were hand-picked from crushed rocks, washed in distilled water in an ultrasonic bath, and dried to avoid dust adsorbed on surface grains. Several grains have been taken for each sub-sample. The crystallinity, purity and composition were checked by XRD on aliquots (see Research data). The reflexion line at ~3.10A on XRD pattern was used to identify the presence of coronadite group minerals and/or pyrolusite. In addition, each grain was investigated by SEM to control the degree of purity. Grains containing inclusions of minerals were discarded from the selection. Based on XRD and SEM analysis, we were able to select eight grains of pure romanechite and of sufficient size (3 to 7 mm) to ensure high bulk potassium (see SEM view of the selected grains in Appendix A). Four samples (15ROM05, 13, 20b and 23) have been duplicated to compare the results. A total of 12 grains have been analysed from the 8 sub-samples. $^{40}Ar/^{39}Ar$ step-heating analyses were performed with a CO_2 laser probe coupled with a MAP 215 mass spectrometer, using the procedure described by Ruffet *et al.* (1991, 1995, 1996, 1997). Irradiation of samples was performed at McMaster Nuclear Reactor (Canada) in the 8C facility and lasted 150 h with a global efficiency (J/h) of 8.15×10^{-5} h^{-1}. The irradiation standard was sanidine TCRs (28.608 ± 0.033 Ma; Renne *et al.*, 1998, 2010 and 2011). Blank analyses were performed routinely before the first and after three to four runs, and were subtracted from the subsequent sample gas fractions. Apparent age errors were plotted at the 1σ level. These ages do not include errors on the $^{40}Ar^{*}/^{39}Ar_K$ ratio and age of the monitor and decay constants. Plateau ages were calculated only if 70% or more of the $^{39}Ar_K$ was released in at least three or more contiguous steps that yielded apparent ages within the 1σ of the integrated age of the plateau segment. Pseudo-plateau ages were defined with the same criteria if the plateau-segment contained less than 70% of the $^{39}Ar_K$ released (Cheilletz et al., 1999). The errors on the $^{40}Ar^{*}/^{39}Ar_K$ ratio and age of the monitor and decay constants were included in the final calculation of the errors of the (pseudo-) plateau ages. Analytical data and parameters used for calculations, such as isotopic ratios measured on pure K and Ca salts, mass discrimination, atmospheric argon ratios, J parameter, decay constants are in the electronic supplementary data material.

5. Results

5.1 Petrography, mineral chemistry and paragenetic sequence

The Mn ore is composed of romanechite with colloform texture (Fig. 3a) constituted by aggregates of micrometric needles (usually 10-1000 µm length) (Fig. 3d), dendrites (Fig. 3e), or tabular crystals (Fig. 3f). Most of the romanechite grows onto the gangue minerals and host granite breccia (Figw. 3c and 3g). Small voids often remain empty (Fig. 3g). Colloform romanechite displays growth bands of slightly variable compositions (Figs. 3d and g) attributed to variations in the amounts of Ba, W and H_2O. Two generations of romanechite are identified with crosscutting relations (Figs. 3h and i). The first generation (rmn-1) is Ca-rich, when rmn-2 has no particular geochemical feature. Romanechite is a vein-filling mineral, meaning that no replacement texture has been observed or described, i.e. by replacement of Mn-rich carbonates or silicates. Romanechite is ubiquitous but some samples contain small amounts of cryptomelane, coronadite and hollandite. These minerals occur as veinlets or as filling of remaining voids in romanechite (Fig. 3h). Pyrolusite is observed as tiny aggregates of bipyramidal laths within the romanechite matrix (Fig. 3j). Hematite is early with respect to romanechite (Fig. 3k).

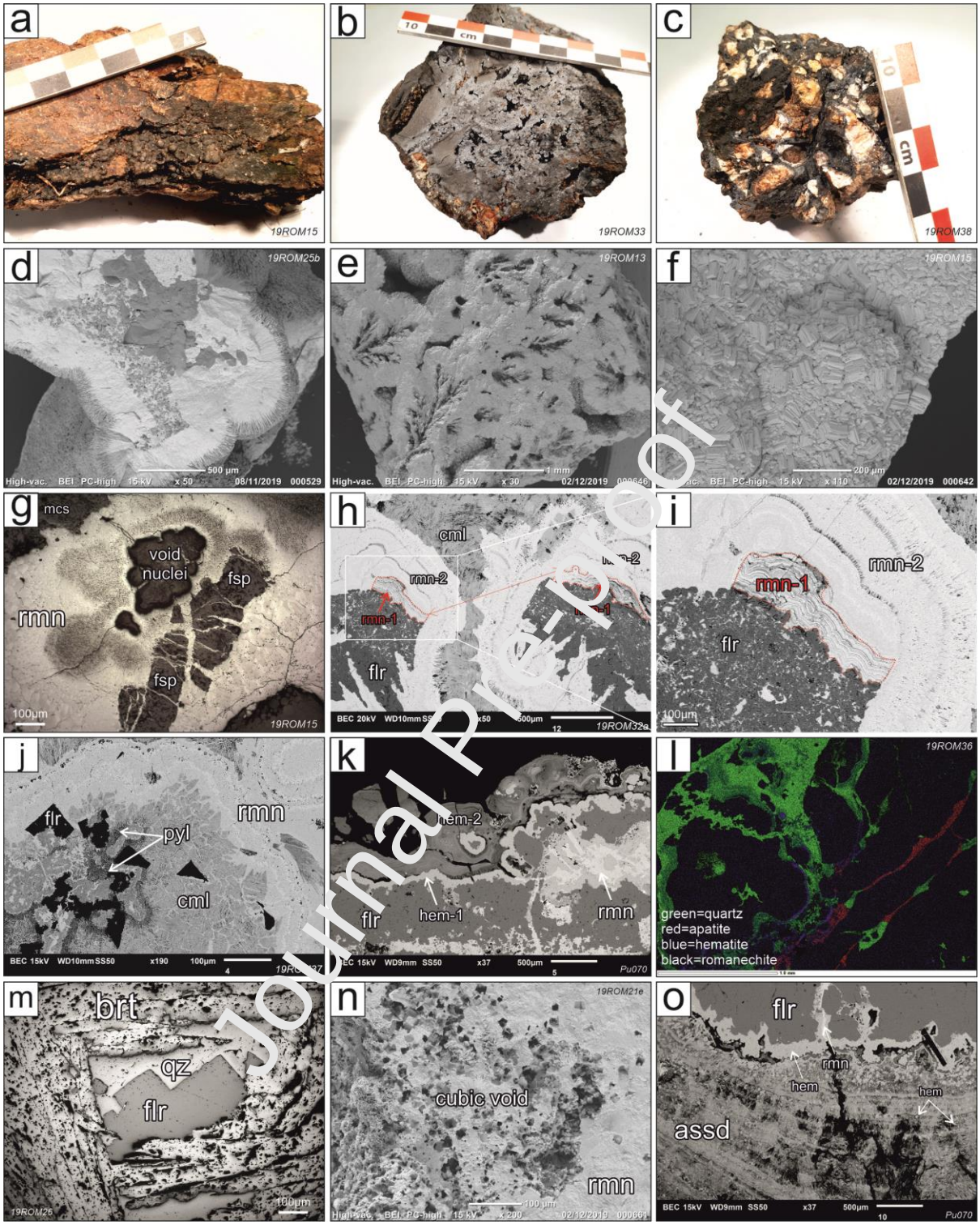

Fig. 3. Petrographic observation of the romanechite-rich ore of Romanèche. **a.** Hand specimen of Mn crust in the host granite at the Les Espagnes deposit. **b.** Hand specimen of the massive Mn ore from the Romanèche deposit. **c.** Hand specimen of the Mn ore breccia containing fragments of the host granite. **d.** Back-scattered electron (BSE) view of colloform romanechite around a quartz-fluorite nuclei. **e.** SEM-BSE view of typical dendrites of romanechite. **f.** SEM-BSE view of prismatic tabular crystals of romanechite (dated sample).

g. Cross-polarized view of romanechite surrounding feldspars and voids (fluorite?) under reflected light. **h.** SEM-BSE view of two colloform generations of romanechite: rmn-1 is brecciated and enclosed in rmn-2. Cryptomelane veinlets split the romanechite matrix into two parts. **i.** Close-up of Fig. 3e showing details of successive generations of romanechite growing onto the fluorite gangue. **j.** SEM-BSE view of pyrolusite between fluorite and romanechite-cryptomelane. **k.** SEM-BSE view of successive crystallization layers of hematite and its relation with gangue minerals and romanechite. **l.** Combined chemical maps of Si (green; quartz), P (red; apatite), Fe (blue; hematite) and Mn (black; romanechite) showing late veins of quartz and apatite. **m.** Cross-polarized view of barite, quartz and fluorite under reflected light. **n.** SEM-BSE view of romanechite hosting cubic voids of former fluorite. **o.** SEM-BSE view of arseniosiderite growing onto hematite and crosscutting relation with romanechite. rmn = romanechite, fsp = feldspar, cml = cryptomelane, flr = fluorite, pyl = pyrolusite, hem = hematite, brt = barite, assd = arseniosiderite.

Gangue minerals are predominantly quartz and fluorite. Barite is also frequent, whereas arseniosiderite [$Ca_2Fe_3(AsO_4)_3O_2.3(H_2O)$] and apatite are relatively scarce. Several generations of quartz are observed: one is younger than romanechite, whereas the other postdates the Mn oxides in fractures with the apatite veins (Fig. 3l). Purple fluorite, when associated with Mn oxides, but colourless or green in unmineralized samples, forms typical cubic crystals (Figs. 3j and m). Fluorite grows onto barite laths prior to ore-forming minerals and quartz (Fig. 3m). Some authors identified fluorite crystals coating the second generation of quartz (Drouot, 1857), some of the fluorite coating romanechite (Chermette, 1975). In heavily mineralized samples, we suspect that some cubic voids (Fig. 3n) were initially fluorite ghosts. Arseniosiderite forms fibrous crystals growing onto hematite and is intersected by romanechite (Fig. 3o).

These petrographic observations show that barite, fluorite and quartz gangue minerals form early and successively in the paragenetic sequence (Figs. 3m and 4). The Fe stage occurs at depth with hematite and arseniosiderite. Romanechite is the highly dominant Mn oxide. Romanechite is late in the paragenetic sequence and likely coeval or younger to the fluorite stage: fluorite can either predate or postdate romanechite. In the latter case, this might be coeval with partial dissolution of the first fluorite generation. Pyrolusite and coronadite group minerals accompany the massive romanechite stage, forming the Mn ore. Apatite, barite and quartz have (re)crystallized later (Fig. 4).

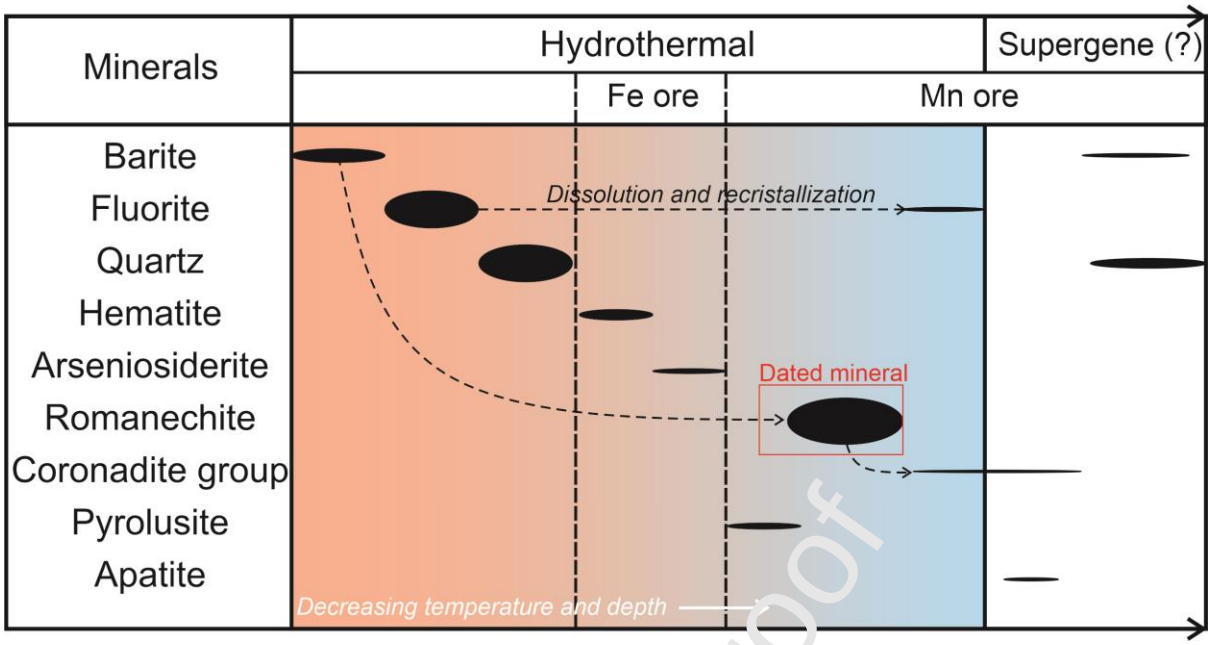

Fig. 4. Paragenetic sequence of the Romanèche Mn deposit based on petrographic observations and SEM analyses.

Crystallographic site occupancy has been determined according to Turner and Post (1988): high ionic radii cations (Ba, H_2O, K, Ca, Na, Sr) occupy the tunnel, when the others (As, W, Si, Al, Fe^{3+}, Cu, Co, Pb, Zn) may substitute to Mn^{3+} in the [MnO_6] octahedra. We calculated structural formulae using the charge-base method with 20 neutralising charges in the theoretical formulae of romanechite [$Ba_{0.66}Mn^{4+}_{3.68}Mn^{3+}_{1.32}O_{10}.1.34.H_2O$]. The amount of H_2O is deduced from the full tunnel site occupancy (=2) and averaged at 4.78 wt.% H_2O. The studied samples deviate from the theoretical formula of romanechite by high amounts of W (0-2.4 wt.% W) and As (0-0.7 wt.%). The amount of K is between 0.01 and 0.26 wt.% K. Finally, the average structural formulae of romanechite from 33 EPMA points is $[Ba_{0.54}Ca_{0.04}Sr_{0.02}Na_{0.02}K_{0.01}(Mn_{4.57}W_{0.03}Al_{0.05}As_{0.02}Fe_{0.02})O_{10}.1.37H_2O$.

5.2 Whole rock geochemistry of the Mn(-F) ore

The host granite has a felsic composition with 69.9 to 74.2 wt.% SiO_2. This silica content is enhanced by silicification and weathering. The MnO concentration is low, ranging between 0.02 and 0.04 wt.%. The other major elements have variable concentrations. Arsenic (17-48 ppm As) and tungsten (15-20 ppm W) are relatively high in comparison with the Upper Continental Crust (Fig. 5a). Rare Earth Elements profiles normalized on the Upper Continental Crust are flat (Fig. 5b).

The major element contents of the Mn ore are MnO (0.03-58.9 wt.%), F (0-42.2 wt.%), CaO (0.2-63.6), SiO_2 (0.4-89.1 wt.%), Fe_2O_3 (0.3-16.0 wt.%) and Ba (1.1-24.8 wt.%). The low MnO value is due to high content of the gangue minerals. Some elements, usually considered as trace elements show high concentrations; W (5-13,200 ppm), As (16-6,760 ppm) and Sr (364-3,337 ppm Sr). Tungsten is hosted by romanechite (Table 1). The other metals are slightly enriched (Co, Cu, Zn; Table 2; Fig. 5a). Rare Earth Elements are not enriched (19.7-95.0 ppm REE) compared to the UCC, characterized by flat patterns with a slight negative Ce anomaly (Table 1; Fig. 5b).

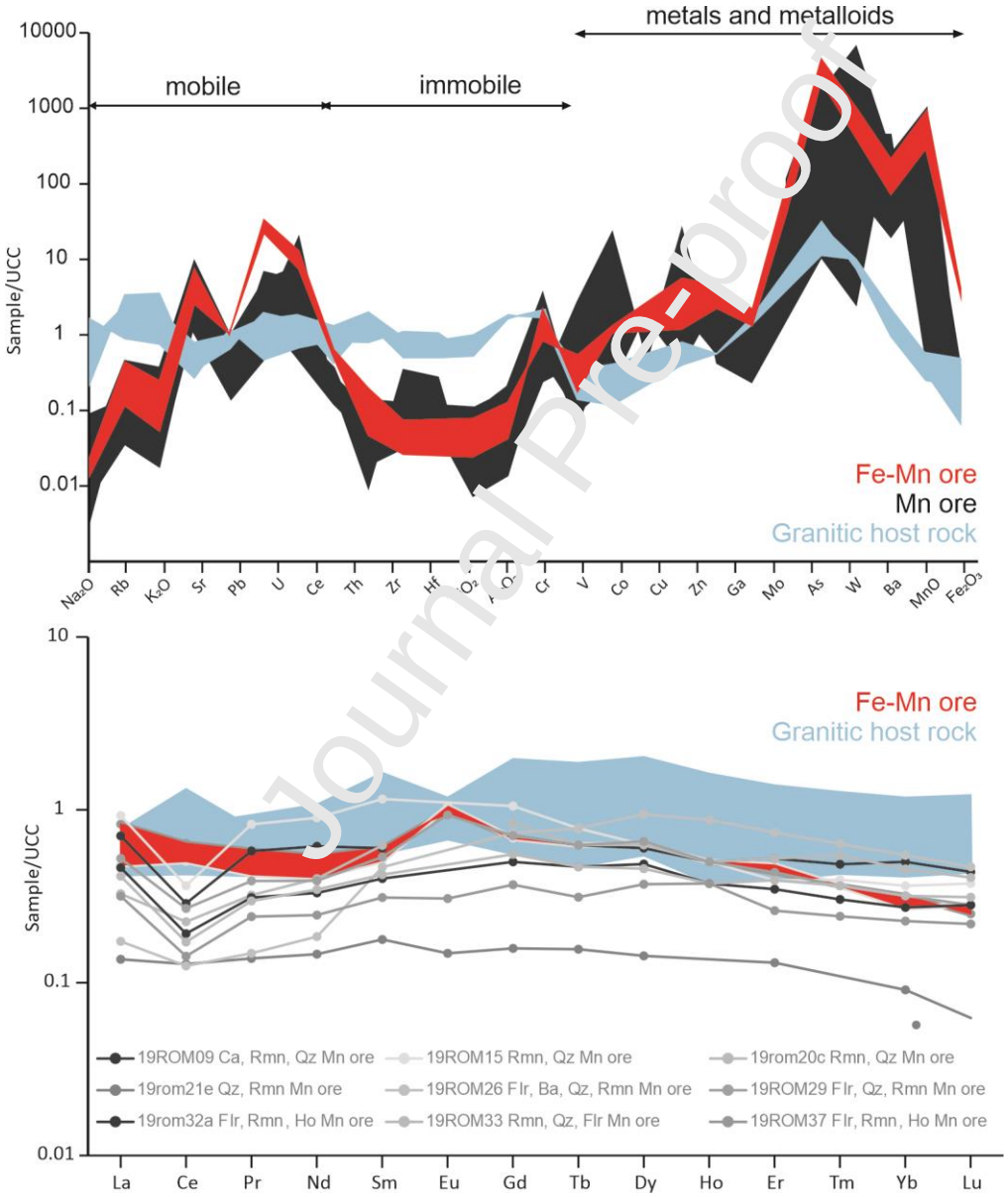

Fig. 5. Geochemistry of the Mn ore, Fe-Mn ore and host rocks compared to the Upper Continental Crust (UCC; McLennan, 2001). **a.** Trace element patterns of the romanechite-bearing Mn ore, Fe-Mn ore and granitic basement rocks in the Romanèche deposit. **b.** Rare

Earth Element patterns of the Mn ore, Fe-Mn ore and host rocks. Ca: calcite; Rmn: romanechite; Qz:quartz; Flr: fluorite; Brt: barite.

5.3 $^{40}Ar/^{39}Ar$ geochronology

$^{40}Ar/^{39}Ar$ analyses of romanechite provide ages spanning the period between late Chattian to Burdigalian (18.2-25.3 Ma; Fig. 6; Table 3).

$^{40}Ar/^{39}Ar$ age spectra (Fig. 6; Table 3) yields five plateau ages at 18.2 ± 0.5 Ma [19ROM30; 85.9% of total $^{39}Ar_K$ released and mean square of weighted deviates (MSWD)=0.26], 23.0 ± 0.4 Ma (19ROM05; 92.1% of total $^{39}Ar_K$ released and MSWD=0.74), 23.4 ± 0.5 Ma (19ROM20b; 86.2% of total $^{39}Ar_K$ released and MSWD=0.05), 23.5 ± 0.4 Ma (19ROM29; 84.3% of total $^{39}Ar_K$ released and MSWD=0.54) and 25.2 ± 0.3 Ma (19ROM21a; 94.3% of total $^{39}Ar_K$ released and MSWD=0.44) and a concordant pseudo-plateau age at 22.8 ± 0.3 Ma (61.2% of total $^{39}Ar_K$ released and MSWD=0.26) provided by duplicate experiment performed on sample 19ROM05. These plateau ages are validated by the processing in the inverse isochron diagrams (correlation diagram) ($^{36}Ar/^{40}Ar$ vs. $^{39}Ar_K/^{40}Ar^*$; Hanes et al., 1985; Roddick et al., 1980; Turner, 1971) with initial ratios $(^{40}Ar/^{36}Ar)_i$ indistinguishable from the atmospheric ratio ($^{40}Ar/^{36}Ar$ = 295.56 according to Lee et al. (2006)) and MSWDs in accordance with the statistical validity criteria. All these experiments provide rather flat $^{37}Ar_{Ca}/^{39}Ar_K$ (# Ca/K) spectra with ratios in the range 0.6–1.2. Note that the $^{37}Ar_{Ca}/^{39}Ar_K$ (# Ca/K) ratios calculated for romanechite are significantly higher than those usually observed for Mn oxides of the coronadite group (~0.1). These ages are consistent with those of Hautmann and Lippolt (2000) at 25.8±0.4, 24.9±0.4, 20.9±0.7 and 20.8±0.6 Ma.

Table 2 Summary of significant geochronological information and validated plateau ages (PA) and Isochron ages based on $^{40}Ar/^{39}Ar$ and $^{37}Ar_{Ca}/^{39}Ar_K$ spectra and Inverse isochron (correlation) diagrams ($^{36}Ar_{atm}/^{40}Ar_{atm}$ vs. $^{39}Ar_K/^{40}Ar^*$) of romanechite in the Romanèche deposit.

Label	Ore type	PA (Ma)	± 1 σ	Isochron age (Ma)	± 1 σ	(40Ar/36Ar)i	± 1 σ	Comments	Reference
RF4a1-k		20.9	0.73					Plateau	Hautmann and Lippolt (2000)
RF4a2		20.8	0.					Plateau	Hautmann and

-k			6						Lippolt (2000)
RF4b-k		24.9	0.39					Plateau	Hautmann and Lippolt (2000)
RF1-k	Collofor m	25.8	0.38					Plateau	Hautmann and Lippolt (2000)
19ROM05-1	Stockwo rk	22.8	0.3	22.7	2.7	296.3	17.2	Plateau	This study
19ROM05-2		23	0.5	23.2	0.6	297.5	2.9	Plateau	This study
19ROM13	Crust	-	-	-	-	-	-	Contamination by old material	This study
19ROM15	Crust	-	-	-	-	-	-	Contamination by old material	This study
19ROM20b-1	Massive	23.4	0.5	23.4	0.9	298.5	2.6	Plateau	This study
19ROM20b-2		-	-	-	-	-	-	Saddle, contamination	This study
19ROM21a	Stockwo rk	25.2	0 3	25.2	0.4	298.6	0.9	Plateau	This study
19ROM23	Stockwo rk	-	-	-	-	-	-	Saddle, contamination	This study
19ROM29	Breccia fragmen t	23.5	0.4	23.8	1.3	296.2	14	Plateau	This study
19ROM30	Massive	18.2	0.5	18.7	0.8	296.9	1.9	Staircase - Ca-rich	This study

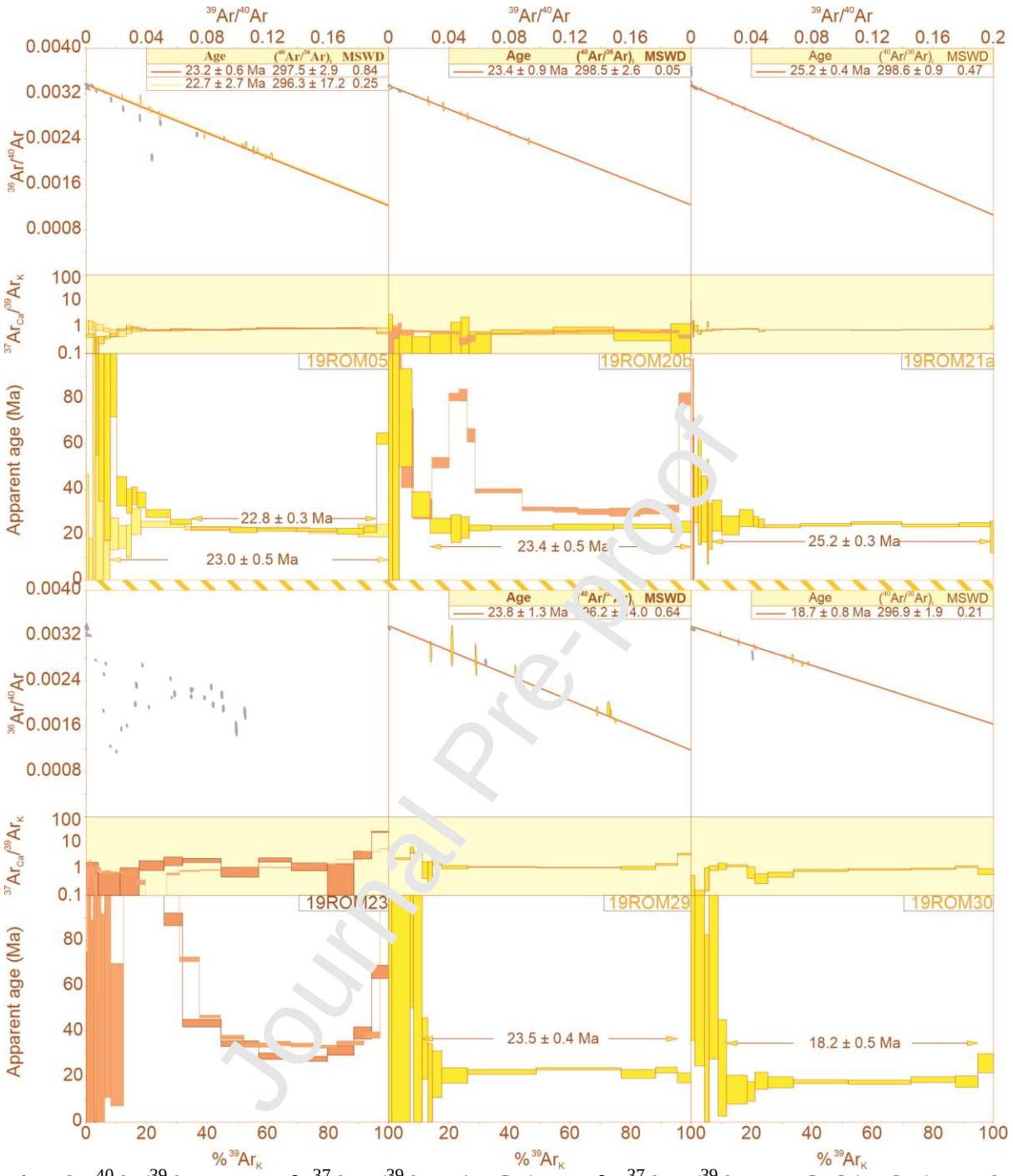

Fig. 6. $^{40}Ar/^{39}Ar$ age and $^{37}Ar_{Ca}/^{39}Ar_K$ (# Ca/K with $^{37}Ar_{Ca}/^{39}Ar_K$ = CaO/K_2O / 2.179; (Deckart et al., 1997) spectra and inverse isochron ($^{36}Ar/^{40}Ar$ vs. $^{39}Ar/^{40}Ar$) diagrams of romanechite samples 19ROM05, 20b, 21a, 23, 29 and 30 from Romanèche deposit. Detailed results are present in supplementary data. Apparent age error bars are at the 1σ level; errors in the J-parameter are not included. Plateau, pseudo-plateau and isochron ages are given with 1σ uncertainties and include errors in the J-parameter. Grey ellipses are excluded from isochron regression, MSWD stands for Mean Squares of Weighted Deviates.

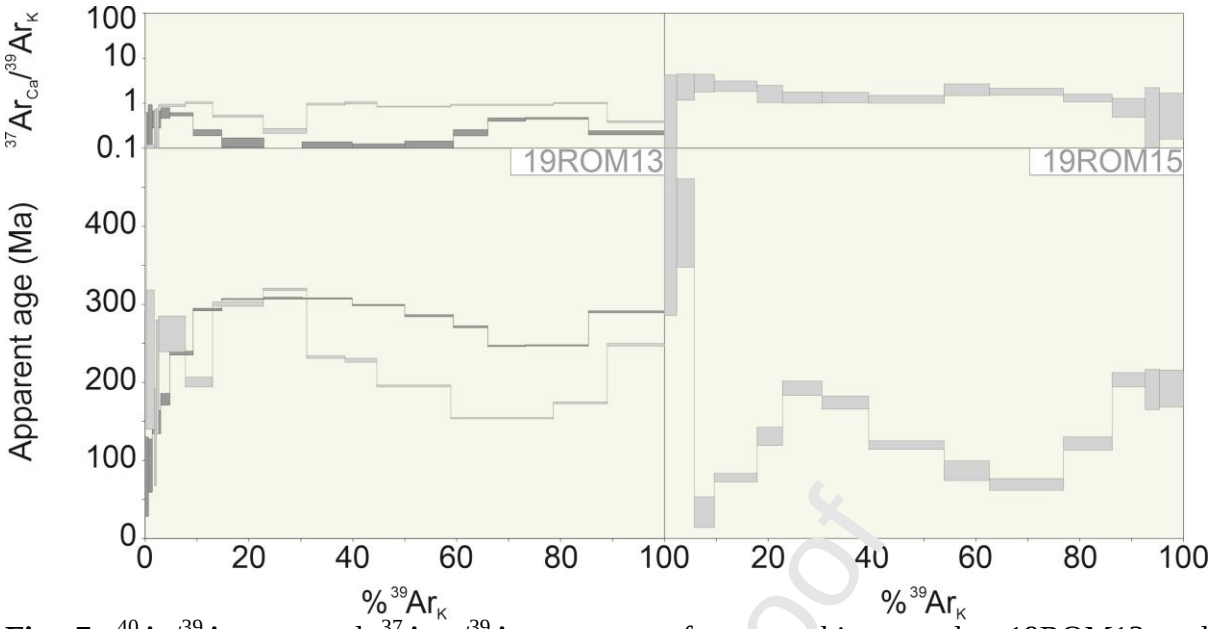

Fig. 7. $^{40}Ar/^{39}Ar$ age and $^{37}Ar_{Ca}/^{39}Ar_K$ spectra of romanèchite samples 19ROM13 and 19ROM15 from Romanèche deposit.

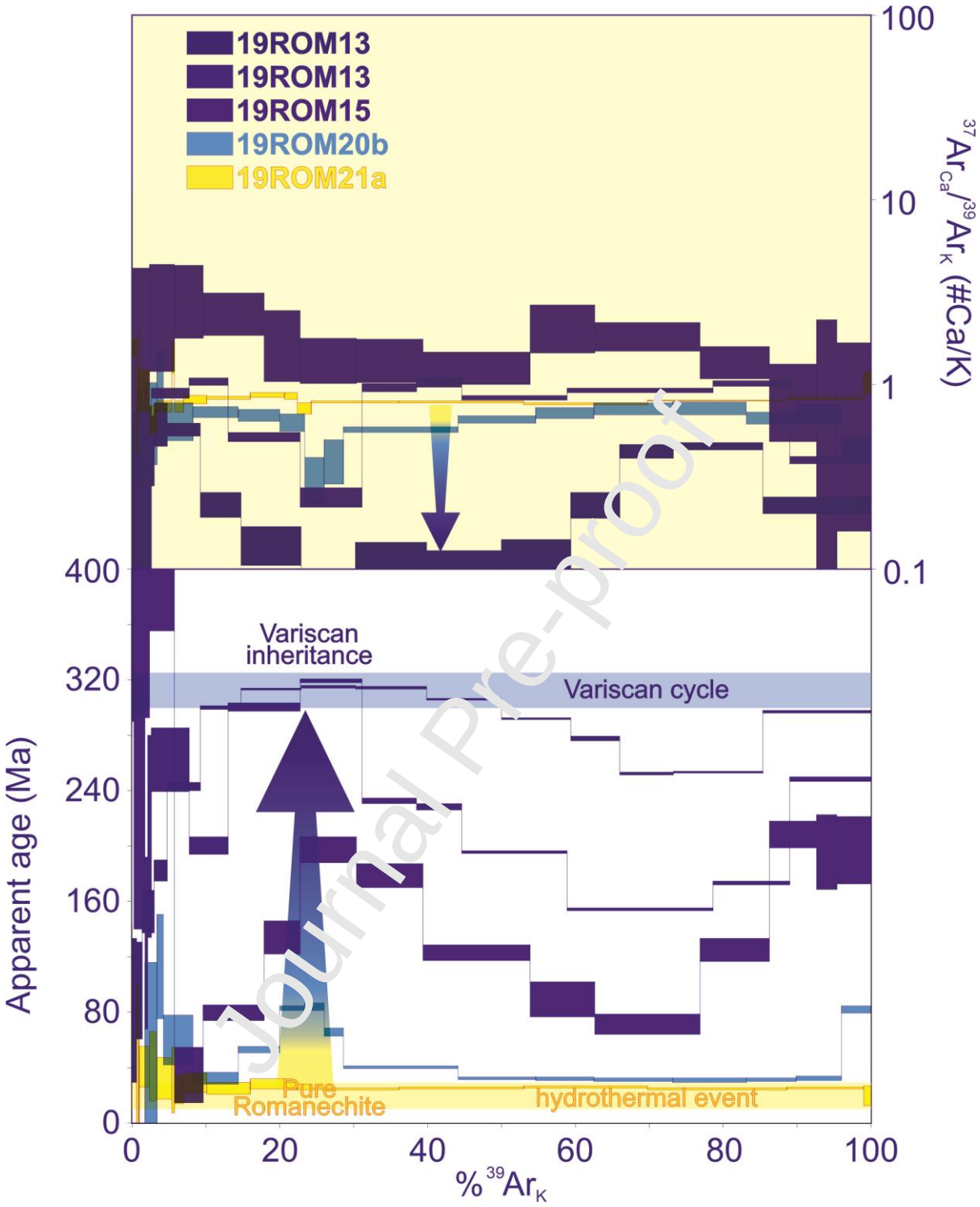

Fig. 8. Compilation of age spectra showing the inverse correlation in the low to intermediate temperature degassing domain between apparent ages and $^{37}Ar_{Ca}/^{39}Ar_K$ (# Ca/K) ratios.

The low-temperature steps (0-10% of $^{39}Ar_K$) of these age spectra are characterised by notably high rates and amounts of atmospheric argon, as shown by the clusters of points along the $^{36}Ar/^{40}Ar$ axis of the inverse isochron diagrams, as well as by anomalously high apparent ages that decrease rapidly (Fig. 6). These low temperature disturbances could express the

degassing of poorly crystallized phases or very small crystallites affected by $^{39}Ar_K$ recoil during the irradiation process (Ruffet et al., 1996; Vasconcelos, 1999).

Analyses of samples 19ROM13, 19ROM15 and duplicate 19ROM20b (19ROM20b-2) produce disturbed age spectra with low to high temperature steps that trace a hump followed by a saddle (Fig. 7). Maximum apparent ages from duplicate analyses of romanechite from sample 19ROM13, which cannot exceed the age of Jurassic carbonates, are consistent with the age of the host granite, at c. 320 Ma, and suggest contamination by Variscan material, probably K-feldspars, which was not detected during the Mn oxide selection process. The shape of their $^{37}Ar_{Ca}/^{39}Ar_K$ (# Ca/K) spectra is antithetical, with the lowest ratios (about 0.1) yielded by steps with the oldest apparent ages and conversely for the highest ratios (about 1) which are provided by the constitutive steps of the saddle basements (Fig. 7). These observations suggest that the first stage of the degassing of these samples is dominated by the contaminating phase, old and Ca-poor, such as K-feldspars, while the second stage is dominated by degassing of the romanechite, younger and Ca-rich. This interpretation most likely applies to all the disturbed age spectra identified in this study, which have similar shapes but with varying amplitudes depending on the relative proportions of contaminating and romanechite phases, as shown in Figure 8. The decrease of the apparent age and the progressive attenuation of their sigmoidal shape are correlated with the progressive increase and flattening of the corresponding $^{37}Ar_{Ca}/^{39}Ar_K$ spectra. This trend leads to perfectly flat age and $^{37}Ar_{Ca}/^{39}Ar_K$ spectra that show the degassing of pure romanechite (e.g., 19ROM21a; Fig. 8), free of any Variscan contamination. The slightly higher values of the $^{37}Ar_{Ca}/^{39}Ar_K$ ratios of romanechite 19ROM15 and 19ROM23 suggest that fluorite (CaF_2) may have interfered with the outgassing of $^{37}Ar_{Ca}$, artificially increasing the measured Ca/K ratios (Fig. 8).

The new results (Figs. 6 and 9) and those which were obtained by Hautmann and Lippolt (2000) at 25.8±0.4, 24.9±0.4, 20.9±0.7 and 20.8±0.6 Ma cover a period of 7.6 Ma, between 25.8±0.4 Ma and 18.2±0.5 Ma (Fig. 9). It is not possible, at this stage, to determine whether the mineralization process was continuous or discontinuous and whether its duration was fully recorded.

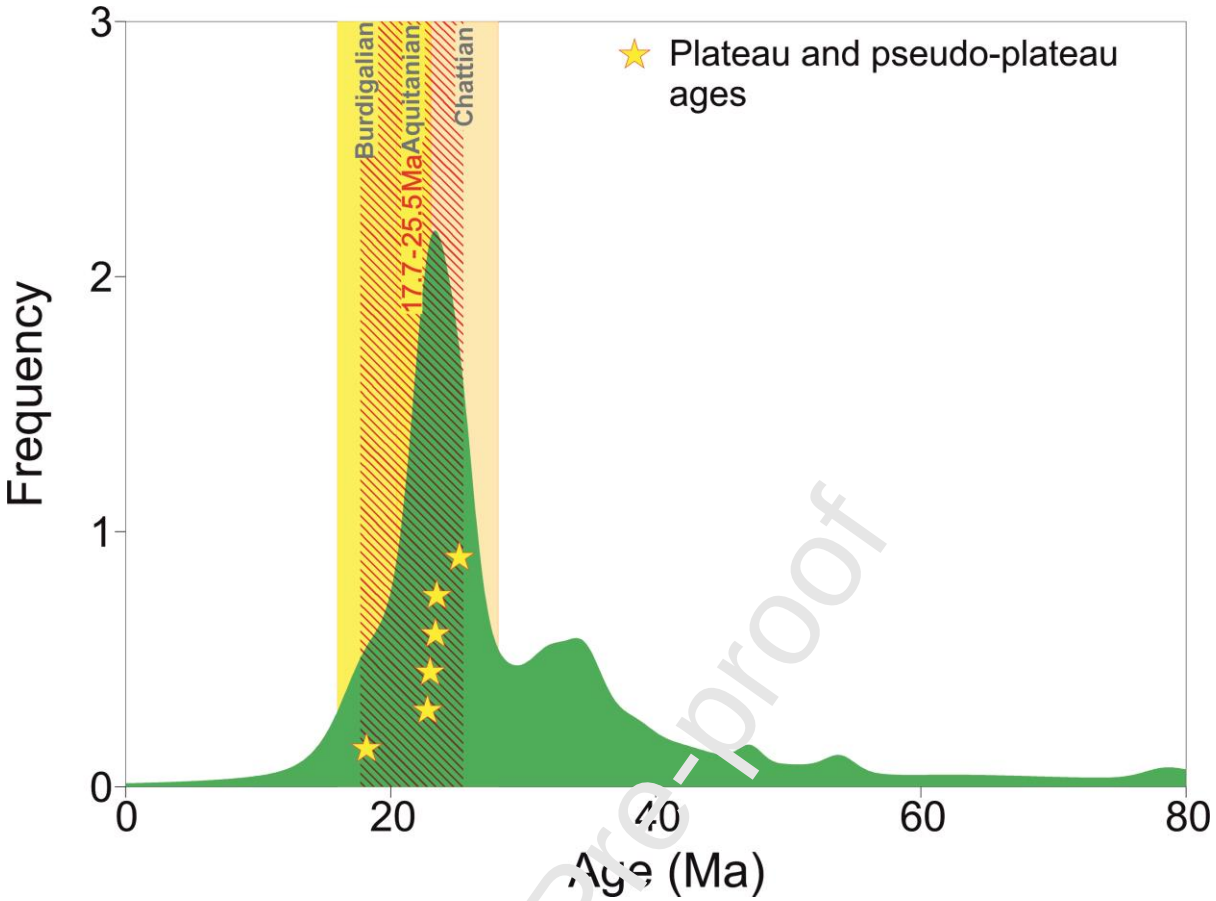

Fig. 9. Frequency (probability density) diagrams of apparent ages of resized age spectra (steps of 5% of $^{39}Ar_K$ released ; see De Putter and Ruffet (2020) and Tremblay et al. (2020) for explanation). Validated ages (plateau and pseudo-plateau ages) are plotted as yellow stars (error bars are smaller than the size of the symbols).

6. Discussion

6.1 Ore deposit model

Romanechite has been described in various environments, from weathering crusts to hydrothermal deposits (Dill, 2010; Nicholson, 1992; Perseil and Pinet, 1976). First considered as a supergene gossan capping an underlying and hidden hydrothermal mineralization (Dolomieu, 1796; Drouot, 1857; Hautmann and Lippolt, 2000; Lacroix, 1910; Lougnon, 1981), the new geochemical and petrographical data from this study support a fault-controlled hydrothermal formation of the romanechite ore.

The fluorite-barite gangue is common in hydrothermal Mn deposits (Hewett, 1966, 1964; Holtstam and Mansfeld, 2001; Leal et al., 2008; Roy, 1981, 1968) whereas it is unusual in other genetic types such as sedimentary, metamorphic or supergene deposits (Dill, 2010; Kuleshov, 2016; Maynard, 2014; Varentsov, 1996). In addition, silicification is the form of

wall-rock alteration associated with the Mn oxide ore (Hewett, 1964). Quartz precipitates either before or after the Mn oxide within the ore zone (Figs. 3i, 3j and 4).

The Mn ore is trapped in and coplanar with the major fault zone (Figs. 1b and 2). Relation with tectonics is expressed in the ore by a breccia composed of granite fragments cemented by romanechite and gangue minerals (Fig. 3c). The Mn ore is itself brecciated and cemented by successive generations of romanechite (Figs. 3h and i). In addition, the clayey zone at the wall of the Mn vein contains fragments of the Jurassic limestones (Lougnon, 1981) and the romanechite ore (Fig. 2, Bouladon, 1958). Accordingly, this fault was active several times before and after the Mn ore deposition.

Dissolution of fluorite inside romanechite (Fig. 3n) and its (re)deposition as a coating on romanechite (Fig. 4, Chermette, 1975) supports that romanechite was formed in the same temperature range than fluorite. These temperatures are most likely between 100-200°C, according to data from other epithermal Mn deposits having similar mineralogical composition (Glasby et al., 2005; Hewett, 1964; Hewett et al., 1963; Hewett and Fleischer, 1960; Leal et al., 2008; Liakopoulos et al., 2001, Madondo et al., 2020; Papavassiliou et al., 2017; Voudouris et al., 2021). The dissolved fluorite crystals observed in some parts of the Romanèche deposit (Fig. 3n) suggests that acidic fluids post-dated romanechite precipitation (Richardson and Holland, 1979; Zhang et al., 2006). Low pH did not remobilize the Mn hosted in romanechite because the high Eh was maintained under prevailing sub-surface conditions.

Mineral zoning is clearly established in space and time with the occurrence of Fe oxides at depth and tetravalent Mn oxides in the upper levels of the mineralization (Fig. 2, Bouladon, 1958). This trend is also materialized by the successive crystallization of hematite, arseniosiderite, romanechite and coronadite group minerals (Fig. 4). The vertical mineral zoning appears to be controlled by the O_2 conditions and cooling of the ascending hydrothermal solution (Hewett, 1966; Perseil and Pinet, 1976). This O_2 and temperature dependency is responsible for the separation of Fe from Mn in the vertical sequence. Seemingly, the Romanèche ore corresponds to the uppermost part of the hydrothermal system as no reduced $Mn^{2+/3+}$-bearing minerals (sulphides, carbonates or silicates) have been reported.

As such, romanechite precipitated in an open system (Figs. 3a, b, c and f), directly from the mineralizing fluid and not by replacement of lower valence Mn-bearing minerals as observed

in other subsurface Mn oxide ores (Dekoninck et al., 2021, 2019, 2016; Lafforgue et al., 2021). In this context, it is unlikely that the romanechite-bearing ore derived from *in situ* supergene weathering such as in gossan.

Geochemical analyses of samples from the Romanèche deposit show an enrichment in Mn-Ba-As-W (Table 1; Fig. 5a), which is consistent with the Mn-As-Ba-Sr enrichment observed in epithermal Mn deposits (Glasby et al., 2005; Hewett et al., 1963). The ternary plot of Bonatti et al. (1972) and the Nicholson's discrimination diagram (Nicholson, 1992) support the hydrothermal origin of the Mn ore, and in particular the strong enrichment in As and other trace metals (Fig. 10, Tables 1 and 2). Nevertheless, these plots cannot be used as a proof of origin because Mn oxides from the supergene zone of polymetallic deposits may also carry a high metal content without being of hydrothermal origin (Vasconcelos, 2002). However, the Romanèche Mn deposit does not contain ore forming minerals hosting high amounts of metals, such as sulphides as the primary source of metals. Instead, the Mn ore is predominantly composed of romanechite and hematite at depth (Fig. 2). Therefore, the geochemistry of the romanechite ore would represent the composition of the fluid from which it has precipitated. In addition, the substantial enrichment in W, up to 1.4 wt.% (Table 1), is consistent with data from hydrothermal epithermal Mn oxide deposits having similar mineralogy and geochemistry (Glasby et al., 2005; Holtstam and Mansfeld, 2001). Tungsten enrichment is usually connected to volcanogenic-magmatic process (i.e. skarns, pegmatite, porphyries, VMS) and has a particular affinity with manganese to form the wolframite series (Dill, 2010). Tungsten-rich romanechite vein-type mineralization hosted in granite may indicate a direct contribution of magmatic fluids in the geochemistry of the ore. Either the low content of W of the mineralizing fluid, the low temperature and the high O_2 fugacity may prevent the precipitation of W-rich minerals, such as wolframite. However, the source of the Mn-Ba-As-W remains elusive, but O_2-poor acidic fluids would transport the metals regardless of their origin.

6.2 Interpretation of romanechite radiometric ages

Hautmann and Lippolt (2000) previously dated four romanechite samples at 25.8±0.4, 24.9±0.4, 20.9±0.7 and 20.8±0.6 Ma which they interpret as a record of a long weathering event (Table 3). However, this interpretation fails to explain some of the key observations described above (Fig. 10): romanechite formed by ascending circulation of hot mineralizing fluids. The new $^{40}Ar/^{39}Ar$ ages between 25.2±0.3 to 18.2±0.5 Ma (Fig. 6) combined with

those obtained by Hautmann and Lippolt (2000) highlight mineralizing events from late Chattian to early Burdigalian (Table 3). It is unlikely that the hydrothermal ore system was active continuously during c. 7.6 My. We rather hypothesize several pulses at ~25 Ma, ~23 Ma, ~21 Ma and ~18 Ma. Therefore, the romanechite ages attest to a regular hydrothermal activity over at least c. 7.6 My along the fault zone delimiting the contact between the MC and the Bresse graben. Therefore, it is also likely that our age data is a testimony of the (re)activation age of the fault system. This study further confirms the reliability of the $^{40}Ar/^{39}Ar$ dating of romanechite in hydrothermal Mn ore.

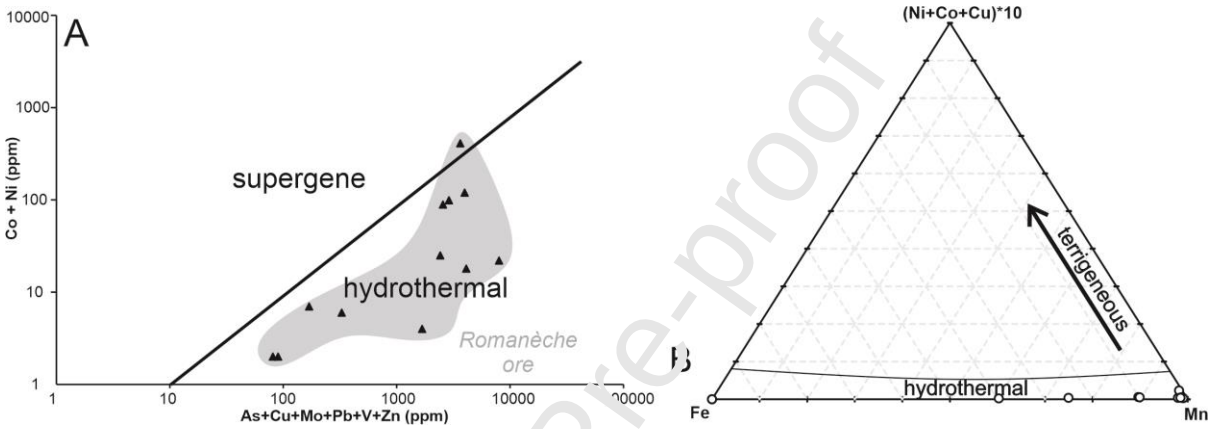

Fig. 10. a. Diagnostic plot of hydrothermal geochemical signature for Mn deposits (Nicholson, 1992) applied to the Romanèche Mn deposit. **b.** Mn-Fe-(Ni+Cu+Co) ternary differentiation diagram (mass basis) for marine hydrogenetic and hydrothermal Mn oxides (Bonatti et al., 1972).

The western part of the European plate was affected by extensive rifting episodes during the Tertiary (Bois, 1993; Prodehl et al., 2006; Ziegler, 1992). E-W extensional stress fields led to the formation of numerous grabens (Eger, Rhine, Limagne, Roanne-Montbrison, Bresse) from the late Eocene to the end of the early Miocene in and around the MC (Merle et al., 1998; Michon and Merle, 2001). The development of this major graben system (West European Rift System; Figs. 1a and b) is accompanied by typical intraplate alkaline volcanism occurring either within the grabens or along their margins (Wilson and Downes, 1991). An important syn-rift magmatism event took place in the northern MC from late Oligocene to early Miocene (Bellon, 1971; Chantepie, 1990; Michon and Merle, 2001) at a time when sedimentation declined in the grabens (Sissingh, 2001, 1998) and where the crust was the thinnest (Merle et al., 1998; Michon and Merle, 2001). This is why most of the late Oligocene volcanic activity is located near the Limagne graben (Fig. 1a) when almost no

volcanic activity occurred elsewhere. The magmatic process involved partial melting in an E-W extensional regime that reactivated N-S Variscan fault zones (Michon and Merle, 2001). The period covered by volcanic activity and reactivation of faults is perfectly coherent with the ~26-18 Ma period recovered from romanechite dating (Table 3).

The high heat flow beneath the MC (Lucazeau et al., 1984), materialized by intraplate magmatic activity probably enhanced circulation of hot mineralizing fluids. We support a primary hydrothermal activity related to the widespread volcanic activity to account for the unusual enrichment in some granitophile elements, such as tungsten (Fig. 5). As indeed high heat flow and widespread volcanism would contribute to hydrothermal activity in the area, we cannot rule out a SedEX-like formation process. The cumulated thickness of ~3,000 meters of Cenozoic sediments in the Bresse Graben (Sissingh, 1998) would account for the generation of basinal fluids by compaction and their upward migration along the margins of the graben. The Mn-Ba-As-W enrichment observed in the romanechite ore (Fig. 5) may have been leached by hydrothermal fluids from the granitic basement rocks. In any case, the bordering fault zone channelled the mineralizing fluid precipitating an epithermal ore type. When these fluids cool and reach more oxygenated wet horizons (i.e., watertable), they precipitated the H_2O-rich Mn oxides (Glasby et al., 2005; Hewett, 1964). The Romanèche area is considered to be subaerial during the deposition of the Mn mineralization (Sissingh, 1998) and likely looked like a hot spring apron system. The Sinemurian carbonates host the epigenetic stratabound mineralization by fluid-rock interaction (Fig. 2).

Overall, it means that other fault-controlled mineralization may also be related to the hydrothermal events reported in this study. This would be true at least for the northern MC domain and possibly in connection with reactivated faults occurring along the West-European graben segments, where Oligocene-Miocene volcanic activity has been reported (i.e., Vosges, Black Forest; Wilson and Downes, 2006).

7. Conclusions

This study provides geochemical, petrographical and geological evidences for hydrothermal origin of the Romanèche manganese deposit. Careful $^{40}Ar/^{39}Ar$ dating of pure romanechite grains provides reliable plateau-ages between 26 Ma and 18 Ma, corresponding to various pulses of hydrothermal activity. This study confirms the great applicability of this mineral for geochronological studies, despite its relatively low K content (0.1-0.6 wt.% K). The good crystallinity of romanechite due to its hydrothermal formation likely favours a better

production and/or retention of the radiogenic argon than poorly crystallized phases of supergene origin. The age of the hydrothermal system of Romanèche is coeval with graben-related fault reactivation and distant volcanic activity in the northern Massif Central, which provides time constrain for fault-related mineralization events along the Massif Central, and possibly along the West-European graben segments.

Acknowledgment

This work was funded and carried out in the framework of the BRGM-TOTAL project Source-to-Sink. We appreciate the help of Prof. J. Wouters and Dr. N. Tumanov of the PC2 platform (UNamur) for collecting XRD patterns. This research also used the resources of the Electron Microscopy Service located at the University of Namur ("Plateforme Technologique Morphologie — Imagerie"). We are delighted to Ir. Pieter L'Hoest of the Department of Materials Engineering at the Katholiek Universiteit Leuven (KUL) for some of the EPMA analyses. We are also delighted to two anonymous reviewers who have greatly improved this manuscript.

Appendix A. Supplementary Material

1. EPMA analytical conditions and standards used for quantification
2. Sample list and main mineralogy
3. Position of the spots collected under back scattered views of samples 19ROM15 and 19ROM32A.
4. BSE views of the grains selected for $^{40}Ar/^{39}Ar$ dating.
5. Hand specimen photographs
6. Field photographs
7. Research data

References

Beauvais, A., Chardon, D., 2013. Modes, tempo, and spatial variability of Cenozoic cratonic denudation: The West African example. Geochemistry, Geophysics, Geosystems 14, 1590–1608. https://doi.org/10.1002/ggge.20093

Bellon, H., 1971. Datation absolue de laves d'Auvergne par la méthode potassium–argon (Ph.D thesis). Université Paris Sud, Orsay.

Bois, C., 1993. Initiation and evolution of the Oligo-Miocene rift basins of southwestern Europe: Contribution of deep seismic reflection profiling. Tectonophysics, The origin of sedimentary basins: Inferences from quantitative modelling and basin analysis 226, 227–252. https://doi.org/10.1016/0040-1951(93)90120-2

Bonatti, E., Kraemer, T., Rydell, H., 1972. Classification and Genesis of Submarine Iron-Manganese Deposits., in: Horn, D.R. (Ed.), Ferromanganese Deposits on the Ocean Floor. National Science Foundation, Washington, DC, pp. 149–166.

Bouladon, J., 1958. Etude sommaire du gisement de manganèse de Romanèche (Saône-et-Loire) (No. A1390-2). Bureau de recherches géologiques, géophysiques et minières, Paris.

Burns, R.G., Burns, V.M., 1979. Manganese oxides, in: Marine Minerals. Mineral Society of America, Washigton DC, pp. 1–46.

Chantepie, M., 1990. Le volcanisme basaltique miocène et pliocène dispersé dans la région de Clermont et sur le plateau des Dômes : étude pétrologique et géochronologique (Mémoire DEA). Université de Clermont-Ferrand, Clermont-Ferrand.

Chantraine, J., Autran, A., Cavelier, C., 2003. Carte géologique de la France à 1/1 000 000.

Cheilletz, A., Ruffet, G., Marignac, C., Kolli, O., Gasquet, D., Féraud, G., Bouillin, J.P., 1999. $^{40}Ar/^{39}Ar$ dating of shear zones in the Variscan basement of Greater Kabylia (Algeria). Evidence of an Eo-Alpine event at 128 Ma (Hauterivian-Barremian boundary): Geodynamic consequences. Tectonophysics 306, 97–116. https://doi.org/10.1016/S0040-1951(99)00047-5

Chermette, A., 1975. L'ancienne mine de manganèse de Romanèche (Saône-et-Loire). Publications de la Société Linnéenne de Lyon 44, 1–11. https://doi.org/10.3406/linly.1975.10171

Choubert, G., Faure-Muret, A., 1973. The Precambrian iron and manganese deposits of the Anti-Atlas, in: Genesis of Precambrian Iron and Manganese Deposits. Presented at the Unesco Earth Sciences Symposium, Kiev, pp. 115–124.

Conly, A.G., Scott, S.D., Bellon, H., 2011. Metalliferous Manganese Oxide Mineralization Associated with the Boléo Cu-Co-Zn District, Mexico. Economic Geology 106, 1173–1196. https://doi.org/10.2113/econgeo.106.7.1173

De Putter, T., Ruffet, G., 2020. Supergene manganese ore records 75 Myr-long Campanian to Pleistocene geodynamic evolution and weathering history of the Central African Great Lakes Region – Tectonics drives, climate assists. Gondwana Research 83, 96–117. https://doi.org/10.1016/j.gr.2020.01.021

Deckart, K., Féraud, G., Bertrand, H., 1997. Age of Jurassic continental tholeiites of French Guyana, Surinam and Guinea: Implications for the initial opening of the Central Atlantic Ocean. Earth and Planetary Science Letters 150, 205–220. https://doi.org/10.1016/S0012-821X(97)00102-7

Decrée, S., Ruffet, G., Putter, T.D., Baele, J.-M., Recourt, P., Jamoussi, F., Yans, J., 2010. Mn oxides as efficient traps for metal pollutants in a polyphase low-temperature Pliocene environment: A case study in the Tamra iron mine, Nefza mining district, Tunisia. Journal of African Earth Sciences 57, 249–261. https://doi.org/10.1016/j.jafrearsci.2009.08.005

Dekoninck, A., Bernard, A., Barbarand, J., Saint-Bezar, B., Missenard, Y., Lepretre, R., Saddiqi, O., Yans, J., 2016. Detailed mineralogy and petrology of manganese oxyhydroxide deposits of the Imini district (Morocco). Mineralium Deposita 51, 13–23. https://doi.org/10.1007/s00126-015-0590-3

Dekoninck, A., Monié, P., Blockmans, S., Hatert, F., Rochez, G., Yans, J., 2019. Genesis and 40Ar/39Ar dating of K-Mn oxides from the Stavelot Massif (Ardenne, Belgium): Insights into Oligocene to Pliocene weathering periods in Western Europe. Ore Geology Reviews 115, 103–191. https://doi.org/10.1016/j.oregeorev.2019.103191

Dekoninck, A., Moussi, B., Vennemann, T., Jamoussi, F., Mattielli, N., Decrée, S., Chaftar, H.-R., Hatira, N., Yans, J., 2018. Mixed hydrothermal and meteoric fluids evidenced by unusual H- and O-isotope compositions of kaolinite-halloysite in the Fe(-Mn) Tamra deposit (Nefza district, NW Tunisia). Applied Clay Science 163, 33–45. https://doi.org/10.1016/j.clay.2018.07.007

Dekoninck, A., Ruffet, G., Missenard, Y., Parizot, O., Magoua, M., Mouttaqi, A., Rochez, Gaëtan, Yans, J., 2021. Multistage genesis of the late Cretaceous manganese karst-hosted Tasdremt deposit (High Atlas, Morocco). Mineralium Deposita 59, 935–956. https://doi.org/10.1007/s00126-020-01017-0

Deng, X.-D., Li, J.-W., Vasconcelos, P.M., 2016. 40Ar/39Ar dating of supergene Mn-oxides from the Zunyi Mn deposit, Guizhou Plateau, SW China: Implications for chemical weathering and paleoclimatic evolution since the late Miocene. Chemical Geology 445, 185–198. https://doi.org/10.1016/j.chemgeo.2016.02.009

Dill, H.G., 2010. The "chessboard" classification scheme of mineral deposits: Mineralogy and geology from aluminum to zirconium. Earth-Science Reviews 100, 1–420. https://doi.org/10.1016/j.earscirev.2009.10.011

Dolomieu, D., 1796. Description de la mine de manganèse de Romanèche. Journal des Mines 2, 14–26.

Drouot, M., 1857. Les gîtes de houille et les terrains des environs des forges et de la Chapelle-sous-Dun et sur les gîtes de manganèse et les terrains des environs de Romanèche. Conseil général des mines, Imprimerie Impériale 109–214.

Dufrénoy, A., 1842. Description de l´arsénio-sidérite, nouvelle espèce d'arséniate de fer. Annales des mines 2, 343–346.

Fusswinkel, T., Wagner, T., Wenzel, T., Wälle, M., Lorenz, J., 2013. Evolution of unconformity-related MnFeAs vein mineralization, Sailauf (Germany): Insight from major and trace elements in oxide and carbonate minerals. Ore Geology Reviews 50, 28–51. https://doi.org/10.1016/j.oregeorev.2012.08.001

Glasby, G.P., Papavassiliou, C.T., Mitsis, J., Valsami-Jones, E., Liakopoulos, A., Renner, R.M., 2005. The Vani manganese deposit, Milos island, Greece: A fossil stratabound Mn−Ba−Pb−Zn−As−Sb−W-rich hydrothermal deposit, in: Developments in Volcanology. Elsevier, pp. 255–291. https://doi.org/10.1016/S1871-644X(05)80045-2

Hanes, J.A., York, D., Hall, C.M., 1985. An $^{40}Ar/^{39}Ar$ geochronological and electron microprobe investigation of an Archaean pyroxenite and its bearing on ancient atmospheric compositions. Canadian Journal of Earth Sciences 22, 947–958. https://doi.org/10.1139/e85-100

Hautmann, S., Lippolt, H.J., 2000. $^{40}Ar/^{39}Ar$ dating of central European K–Mn oxides — a chronological framework of supergene alteration processes during the Neogene. Chemical Geology 170, 37–80. https://doi.org/10.1016/S0009-2541(99)00241-7

Hewett, D.F., 1966. Stratified deposits of the oxides and carbonates of manganese. Economic Geology 61, 431–461. https://doi.org/10.2113/gsecongeo.61.3.431

Hewett, D.F., 1964. Veins of hypogene manganese oxide minerals in the southwestern United States. Economic Geology 59, 1429–1472. https://doi.org/10.2113/gsecongeo.59.8.1429

Hewett, D.F., Fleischer, M., 1960. Deposits of the manganese oxides. Economic Geology 55, 1–55. https://doi.org/10.2113/gsecongeo.55.1.1

Hewett, D.F., Fleischer, M., Conklin, N., 1963. Deposits of the manganese oxides; supplement. Economic Geology 58, 1–51. https://doi.org/10.2113/gsecongeo.58.1.1

Holtstam, D., Mansfeld, J., 2001. Origin of a carbonate-hosted Fe-Mn-(Ba-As-Pb-Sb-W) deposit of Långban-type in central Sweden. Min Dep 36, 641–657. https://doi.org/10.1007/s001260100183

Jean, A., Beauvais, A., Chardon, D., Arnaud, N., Jayananda, M., Mathe, P.E., 2019. Weathering history and landscape evolution of Western Ghats (India) from 40Ar/39Ar dating of supergene K–Mn oxides. Journal of the Geological Society. https://doi.org/10.1144/jgs2019-048

Kuleshov, V., 2016. Isotope geochemistry: the origin and formation of manganese rocks and ores. Elsevier, Amsterdam Boston Heidelberg London New York Oxford Paris San Diego San Francisco Singapore Sydney Tokyo.

Lacroix, A., 1910. Minéralogie de la France et de ses colonies: description physique et chimique des minéraux, étude des conditions géologiques et leurs gisements, Librairie Polytechnique, Ch. Béranger. ed, Tome 4. Librairie Polytechnique, Paris.

Lafforgue, L., Dekoninck, A., Barbarand, J., Brigaud, B., Bouabdellah, M., Verhaert, M., Mouttaqi, A., Yans, J., 2021. Geological and geochemical constrains on the genesis of the sedimentary-hosted Bou Arfa Mn(-Fe) deposit (Eastern High Atlas, Morocco). Ore Geology Reviews 133, 104094. https://doi.org/10.1016/j.oregeorev.2021.104094

Leal, P.R., Correa, M.J., Alpetrano, S.J., Etcheverry, R.O., de Brodtkorb, M.K., 2008. The manganese deposits of the Pampean Ranges, Argentina. The Canadian Mineralogist 46, 1215–1233. https://doi.org/10.3749/canmin.46.5.1215

Lee, J.-Y., Marti, K., Severinghaus, J.P., Kawamura, K., Yoo, H.-S., Lee, J.B., Kim, J.S., 2006. A redetermination of the isotopic abundances of atmospheric Ar. Geochimica et Cosmochimica Acta 70, 4507–4512. https://doi.org/10.1016/j.gca.2006.06.1563

Li, J.-W., Vasconcelos, P., Duzgoren-Aydin, N., Yan, D.-R., Zhang, W., Deng, X.-D., Zhao, X.-F., Zeng, Z.-P., Hu, M.-A., 2007. Neogene weathering and supergene manganese enrichment in subtropical South China: An 40Ar/39Ar approach and paleoclimatic significance. Earth and Planetary Science Letters 256, 389–402. https://doi.org/10.1016/j.epsl.2007.01.021

Liakopoulos, A., Glasby, G.P., Papavassiliou, C.T., Boulegue, J., 2001. Nature and origin of the Vani manganese deposit, Milos, Greece: an overview. Ore Geology Reviews 18, 181–209. https://doi.org/10.1016/S0169-1368(01)00029-4

Lippolt, H.J., Hautmann, S., 1995. $^{40}Ar/^{39}Ar$ ages of Precambrian manganese ore minerals from Sweden, India and Morocco. Mineralium Deposita 30, 246–256. https://doi.org/10.1007/BF00196360

Lougnon, J., 1981. Ressources minières françaises : les gisements de manganèse (Bureau de Recherches Géologiques et Minières No. Tome 10). BRGM.

Lucazeau, F., Vasseur, G., Bayer, R., 1984. Interpretation of heat flow data in the french massif central. Tectonophysics, Terrestrial Heat Flow Studies and the Structure of the Lithosphere 103, 99–119. https://doi.org/10.1016/0040-1951(84)90077-5

Madondo, J., Canet, C., González-Partida, E., Rodríguez-Díaz, A.A., Núñez-Useche, F., Alfonso, P., Rajabi, A., Pi, T., Blignaut, L., Vafeas, N., 2020. Geochemical constraints on the genesis of the 'Montaña de Manganeso' vein-type Mn deposit, Mexican Plateau. Ore Geology Reviews 125, 103680. https://doi.org/10.1016/j.oregeorev.2020.103680

Maynard, J.B., 2014. Manganiferous sediments, rocks, and ores, in: Treatise on Geochemistry. Elsevier, pp. 327–349.

McLennan, S.M., 2001. Relationships between the trace element composition of sedimentary rocks and upper continental crust. Geochemistry, Geophysics, Geosystems 2, 24. https://doi.org/10.1029/2000GC000109

Merle, O., Michon, L., Camus, G., Goer, A. de, 1998. L'extension oligocene sur la transversale septentrionale du rift du Massif central. Bulletin de la Société Géologique de France 169, 615–626.

Michon, L., Merle, O., 2001. The evolution of the Massif Central Rift; spatio-temporal distribution of the volcanism. Bulletin de la Société Géologique de France 172, 201–211. https://doi.org/10.2113/172.2.201

Nicholson, K., 1992. Contrasting mineralogical-geochemical signatures of manganese oxides; guides to metallogenesis. Economic Geology 87, 1253–1264. https://doi.org/10.2113/gsecongeo.87.5.1253

O'Reilly, G.A., 1992. Petrographic and geochemical evidence for a hypogene origin of granite-hosted, vein-type Mn mineralization at the New Ross Mn deposits, Lunenburg County, Nova Scotia, Canada. Economic Geology 87, 1275–1300. https://doi.org/10.2113/gsecongeo.87.5.1275

Papavassiliou, K., Voudouris, P., Kanellopoulos, C., Glasby, G., Alfieris, D., Mitsis, I., 2017. New geochemical and mineralogical constraints on the genesis of the Vani hydrothermal manganese deposit at NW Milos island, Greece: Comparison with the Aspro Gialoudi deposit and implications for the formation of the Milos manganese mineralization. Ore Geology Reviews 80, 594–611. https://doi.org/10.1016/j.oregeorev.2016.07.023

Perseil, E.A., Pinet, M., 1976. Contribution à la connaissance des romanéchites et des cryptomélanes — coronadites — hollandites. Traits essentiels et paragenèses. Contr. Mineral. and Petrol. 55, 191–204. https://doi.org/10.1007/BF00372226

Post, J.E., 1999. Manganese oxide minerals: crystal structures and economic and environmental significance. Proceedings of the National Academy of Sciences 96, 3447–3454. https://doi.org/10.1073/pnas.96.7.3447

Prodehl, C., Mueller, St., Haak, V., 2006. The European Cenozoic rift system, in: Continental Rifts: Evolution, Structure, Tectonics, Developments in Geotectonics. Elsevier, pp. 133–212.

Richardson, C.K., Holland, H.D., 1979. The solubility of fluorite in hydrothermal solutions, an experimental study. Geochimica et Cosmochimica Acta 43, 1313–1325. https://doi.org/10.1016/0016-7037(79)90121-2

Roddick, J.C., Cliff, R.A., Rex, D.C., 1980. The evolution of excess argon in alpine biotites - a 40Ar-39Ar analysis. Earth and Planetary Science Letters 48, 185–208. https://doi.org/10.1016/0012-821X(80)90181-8

Roy, S., 1981. Manganese deposits. Academic Press, London ; New York.

Roy, S., 1968. Mineralogy of the different genetic types of manganese deposits. Economic Geology 63, 760–786. https://doi.org/10.2113/gsecongeo.63.7.760

Ruffet, G., Féraud, G., Amouric, M., 1991. Comparison of 40Ar-39Ar conventional and laser dating of biotites from the North Trégor Batholith. Geochimica et Cosmochimica Acta 55, 1675–1688. https://doi.org/10.1016/0016-7037(91)90138-U

Ruffet, G., Féraud, G., Balèvre, M., Kiénast, J.-R., 1995. Plateau ages and excess argon in phengites: an 40Ar□39Ar laser probe study of Alpine micas (Sesia Zone, Western Alps, northern Italy). Chemical Geology 121, 327–343. https://doi.org/10.1016/0009-2541(94)00132-R

Ruffet, G., Gruau, G., Ballèvre, M., Féraud, G., Philippot, P., 1997. Rb/Sr and $^{40}Ar/^{39}Ar$ laser probe dating of high-pressure phengites from the Sesia zone (Western Alps): underscoring of excess argon and new age constraints on the high-pressure

metamorphism. Chemical Geology 141, 1–18. https://doi.org/10.1016/S0009-2541(97)00052-1

Ruffet, G., Innocent, C., Michard, A., Féraud, G., Beauvais, A., Nahon, D., Hamelin, B., 1996. A geochronological and study of K-Mn oxides from the weathering sequence of Azul, Brazil. Geochimica et Cosmochimica Acta 60, 2219–2232. https://doi.org/10.1016/0016-7037(96)00080-4

Sissingh, W., 2001. Tectonostratigraphy of the West Alpine Foreland: correlation of Tertiary sedimentary sequences, changes in eustatic sea-level and stress regimes. Tectonophysics 333, 361–400. https://doi.org/10.1016/S0040-1951(01)00020-8

Sissingh, W., 1998. Comparative Tertiary stratigraphy of the Rhine Graben, Bresse Graben and Molasse Basin: correlation of Alpine foreland events. Tectonophysics 300, 249–284. https://doi.org/10.1016/S0040-1951(98)00243-1

Tremblay, A., Ruffet, G., Lemarchand, J., 2020. Timing and duration of Archean orogenic gold deposits in the Bourlamaque pluton, Val d'Or mining camp, Abitibi, Canada. Ore Geology Reviews 127, 103812. https://doi.org/10.1016/j.oregeorev.2020.103812

Turner, G., 1971. Argon 40-argon 39 dating: the optimization of irradiation parameters. Earth and Planetary Science Letters 10, 227–234. https://doi.org/10.1016/0012-821X(71)90010-0

Turner, S., Post, J.E., 1988. Refinement of the substructure and superstructure of romanechite. American Mineralogist 73, 1155–1161.

Varentsov, I.M., 1996. Manganese ores of supergene zone: Geochemistry of formation, Solid Earth Sciences Library. Springer Netherlands, Dordrecht.

Vasconcelos, P.M., 2002. Geochronology of Weathering in the Mt Isa and Charters Towers Regions, Northern Queensland (Open File Reports (OFRs) No. 139), CRC for Landscape Evolution & Mineral Exploration (LEME). University of Queensland, St Lucia.

Vasconcelos, P.M., 1999. K-Ar and $^{40}Ar/^{39}Ar$ geochronology of weathering processes. Annual Review of Earth and Planetary Sciences 27, 183–229. https://doi.org/10.1146/annurev.earth.27.1.183

Vasconcelos, P.M., Becker, T.A., Renne, P.R., Brimhall, G.H., 1992. Age and duration of weathering by $^{40}K/^{40}Ar$ and $^{40}Ar/^{39}Ar$ analysis of potassium-manganese oxides. Science 258, 451–455. https://doi.org/10.1126/science.258.5081.451

Vasconcelos, P.M., Carmo, I. de O., 2018. Calibrating denudation chronology through $^{40}Ar/^{39}Ar$ weathering geochronology. Earth-Science Reviews 179, 411–435. https://doi.org/10.1016/j.earscirev.2018.01.003

Vasconcelos, P.M., Heim, J.A., Farley, K.A., Monteiro, H., Waltenberg, K., 2013. 40Ar/39Ar and (U–Th)/He – 4He/3He geochronology of landscape evolution and channel iron deposit genesis at Lynn Peak, Western Australia. Geochimica et Cosmochimica Acta 117, 283–312. https://doi.org/10.1016/j.gca.2013.03.037

Vasconcelos, P.M., Renne, P.R., Becker, T.A., Wenk, H.-R., 1995. Mechanisms and kinetics of atmospheric, radiogenic, and nucleogenic argon release from cryptomelane during analysis. Geochimica et Cosmochimica Acta 59, 2057–2070. https://doi.org/10.1016/0016-7037(95)00126-3

Vasconcelos, P.M., Renne, P.R., Brimhall, G.H., Becker, T.A., 1994. Direct dating of weathering phenomena by $^{40}Ar/^{39}Ar$ and K-Ar analysis of supergene K-Mn oxides. Geochimica et Cosmochimica Acta 58, 1635–1663. https://doi.org/10.1016/0016-7037(94)90565-7

Voudouris, P., Kati, M., Magganas, A., Keith, M., Valsami-Jones, E., Haase, K., Klemd, R., Nestmeyer, M., 2021. Arsenian Pyrite and Cinnabar from Active Submarine Nearshore Vents, Paleochori Bay, Milos Island, Greece. Minerals 11, 14. https://doi.org/10.3390/min11010014

Wilson, M., Downes, H., 2006. Tertiary-Quaternary intra-plate magmatism in Europe and its relationship to mantle dynamics. Geological Society, London, Memoirs 32, 147–166. https://doi.org/10.1144/GSL.MEM.2006.032.01.09

Wilson, M., Downes, H., 1991. Tertiary—Quaternary Extension-Related Alkaline Magmatism in Western and Central Europe. Journal of Petrology 32, 811–849. https://doi.org/10.1093/petrology/32.4.811

Zhang, R., Hu, S., Zhang, X., 2006. Experimental Study of Dissolution Rates of Fluorite in HCl–H2O Solutions. Aquat Geochem 12, 123–159. https://doi.org/10.1007/s10498-005-3658-3

Ziegler, P.A., 1992. European Cenozoic rift system. Tectonophysics 208, 91–111. https://doi.org/10.1016/0040-1951(92)90338-7

Author statement file

We confirm that this manuscript has not been published elsewhere and is not under consideration by another journal. All authors have approved the manuscript and agree with its submission to *Chemical Geology*. AD and GR actively co-written the article main body. JB and RW collected the samples from the field investigation, actively took part of the discussion and carefully revised former versions of the manuscript. S. Philippo helped access to analytical facilities (SEM-EDS), provided key samples of romanechite from the National Museum of Natural History collection and carefully revised former versions of the manuscript. O. Namur and Y. Zhang acquired the EPMA and revised the manuscript.

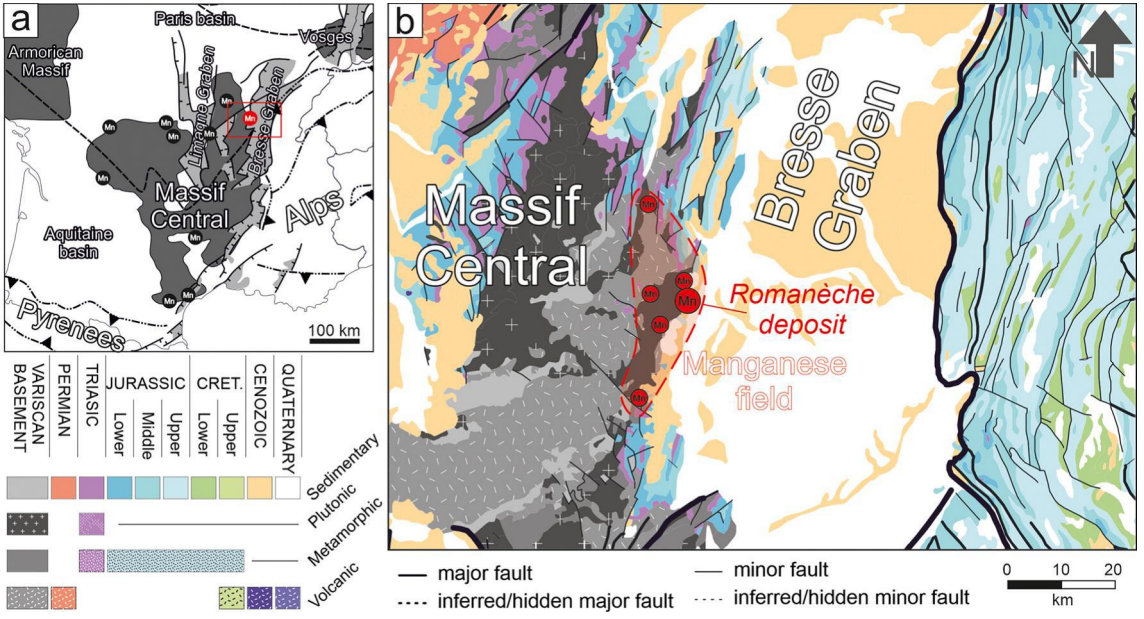
a
Paris basin
Vosges
Armorican Massif
Limagne Graben
Bresse Graben
Massif Central
Alps
Aquitaine basin
Pyrenees
100 km
b
Massif Central
Bresse Graben
N
Romanèche deposit
Manganese field
major fault
inferred/hidden major fault
minor fault
inferred/hidden minor fault
0 10 20
km
VARISCAN BASEMENT
PERMIAN
TRIASIC
JURASSIC
Lower
Middle
Upper
CRET.
Lower
Upper
CENOZOIC
QUATERNARY
Sedimentary
Plutonic
Metamorphic
Volcanic

Figure 1

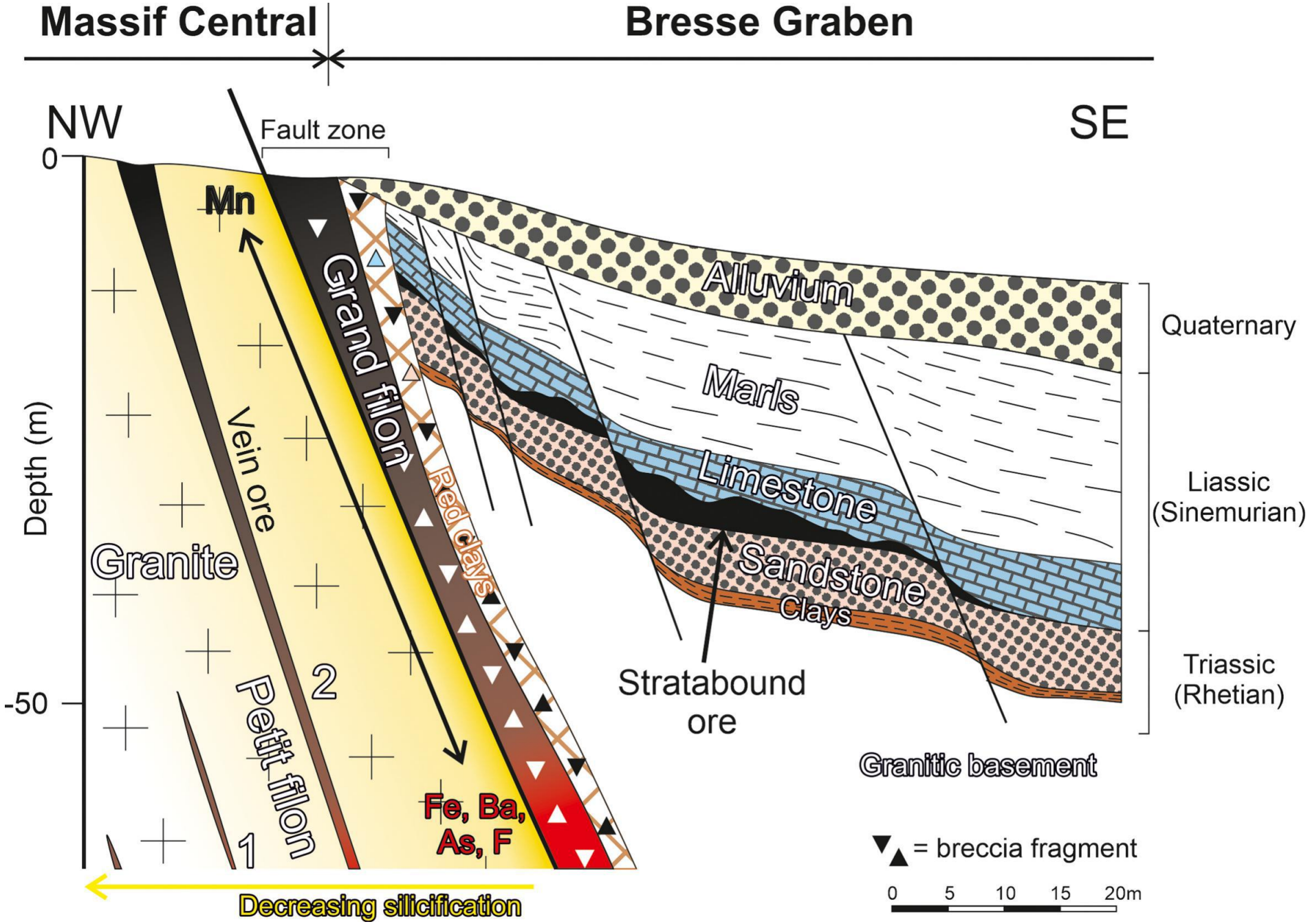
Massif Central
Bresse Graben
NW
SE
Fault zone
0
-50
Depth (m)
Mn
Grand filon
Vein ore
Granite
Petit filon
1
2
Red clays
Fe, Ba,
As, F
Alluvium
Marls
Limestone
Sandstone
Clays
Stratabound
ore
Granitic basement
Quaternary
Liassic
(Sinemurian)
Triassic
(Rhetian)
Decreasing silicification
= breccia fragment
0 5 10 15 20m

Figure 2

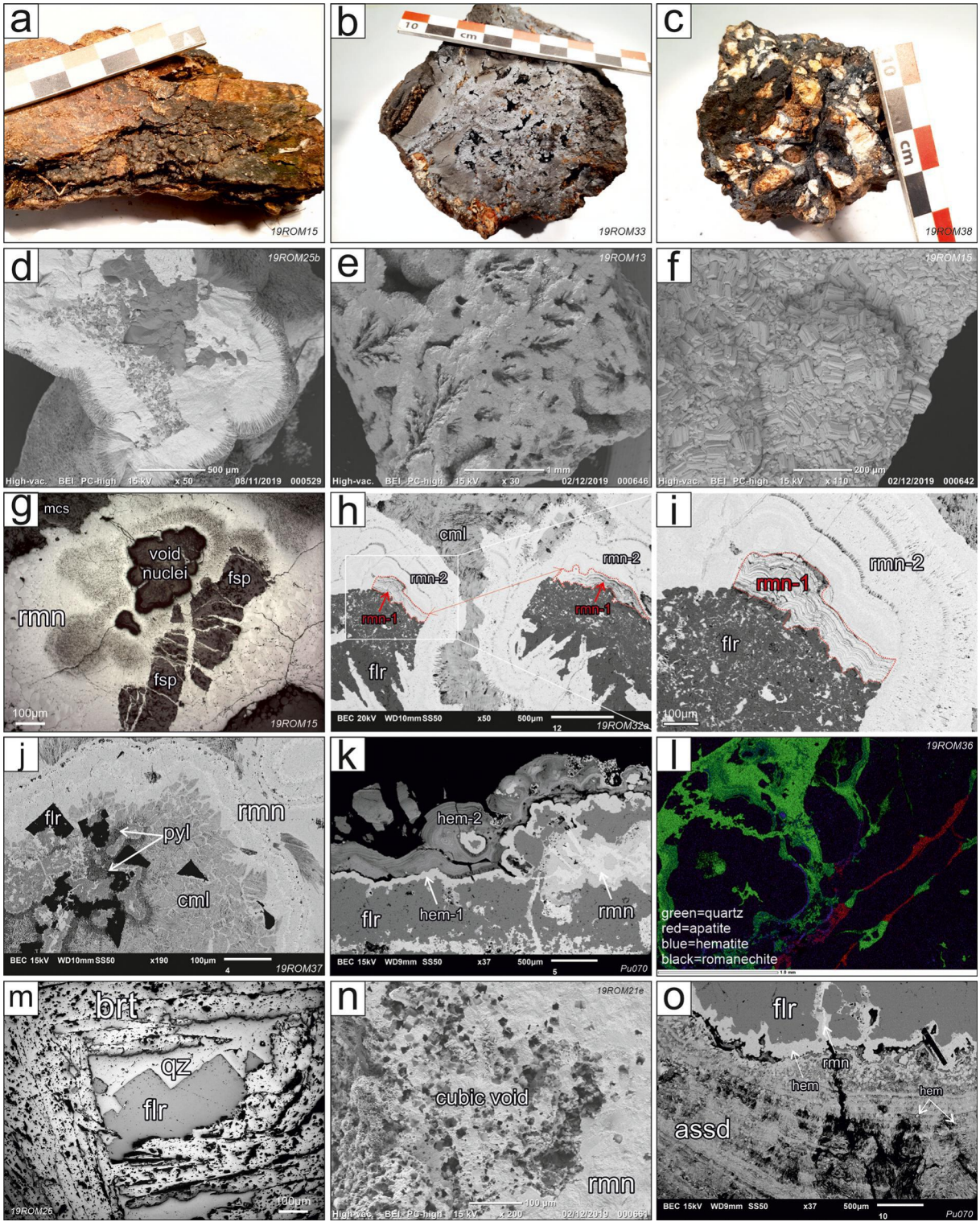
a
19ROM15
b
10
cm
19ROM33
c
10
cm
19ROM38
d
19ROM25b
High-vac. BEI PC-high 15 kV x 50 08/11/2019 000529
500 µm
e
19ROM13
High-vac. BEI PC-high 15 kV x 30 02/12/2019 000646
1 mm
f
19ROM15
High-vac. BEI PC-high 15 kV x 110 02/12/2019 000642
200 µm
g
mcs
void
nuclei
fsp
rmn
fsp
100µm
19ROM15
h
cml
rmn-2
rmn-2
rmn-1
rmn-1
flr
BEC 20kV WD10mm SS50 x50 500µm
12
19ROM32a
i
rmn-2
rmn-1
flr
100µm
j
flr
pyl
rmn
cml
BEC 15kV WD10mm SS50 x190 100µm
4
19ROM37
k
hem-2
flr
hem-1
rmn
BEC 15kV WD9mm SS50 x37 500µm
5
Pu070
l
19ROM36
green=quartz
red=apatite
blue=hematite
black=romanechite
m
brt
qz
flr
19ROM26
100µm
n
19ROM21e
cubic void
rmn
High-vac. BEI PC-high 15 kV x 200 02/12/2019 000661
100 µm
o
flr
rmn
hem
hem
assd
BEC 15kV WD9mm SS50 x37 500µm
10
Pu070

Figure 3

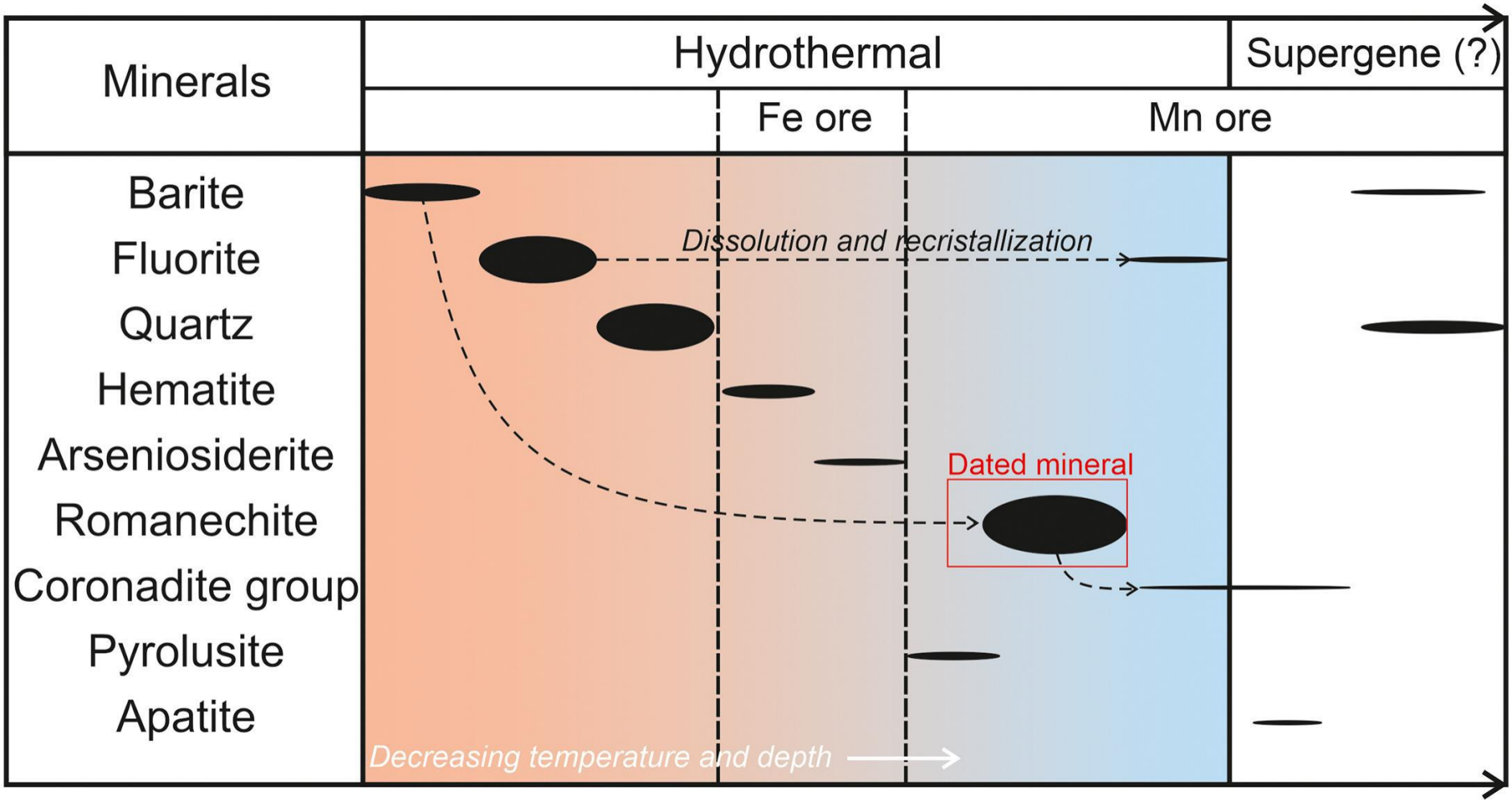
Minerals
Hydrothermal
Supergene (?)
Fe ore
Mn ore
Barite
Fluorite
Quartz
Hematite
Arseniosiderite
Romanechite
Coronadite group
Pyrolusite
Apatite
Dissolution and recristallization
Dated mineral
Decreasing temperature and depth

Figure 4

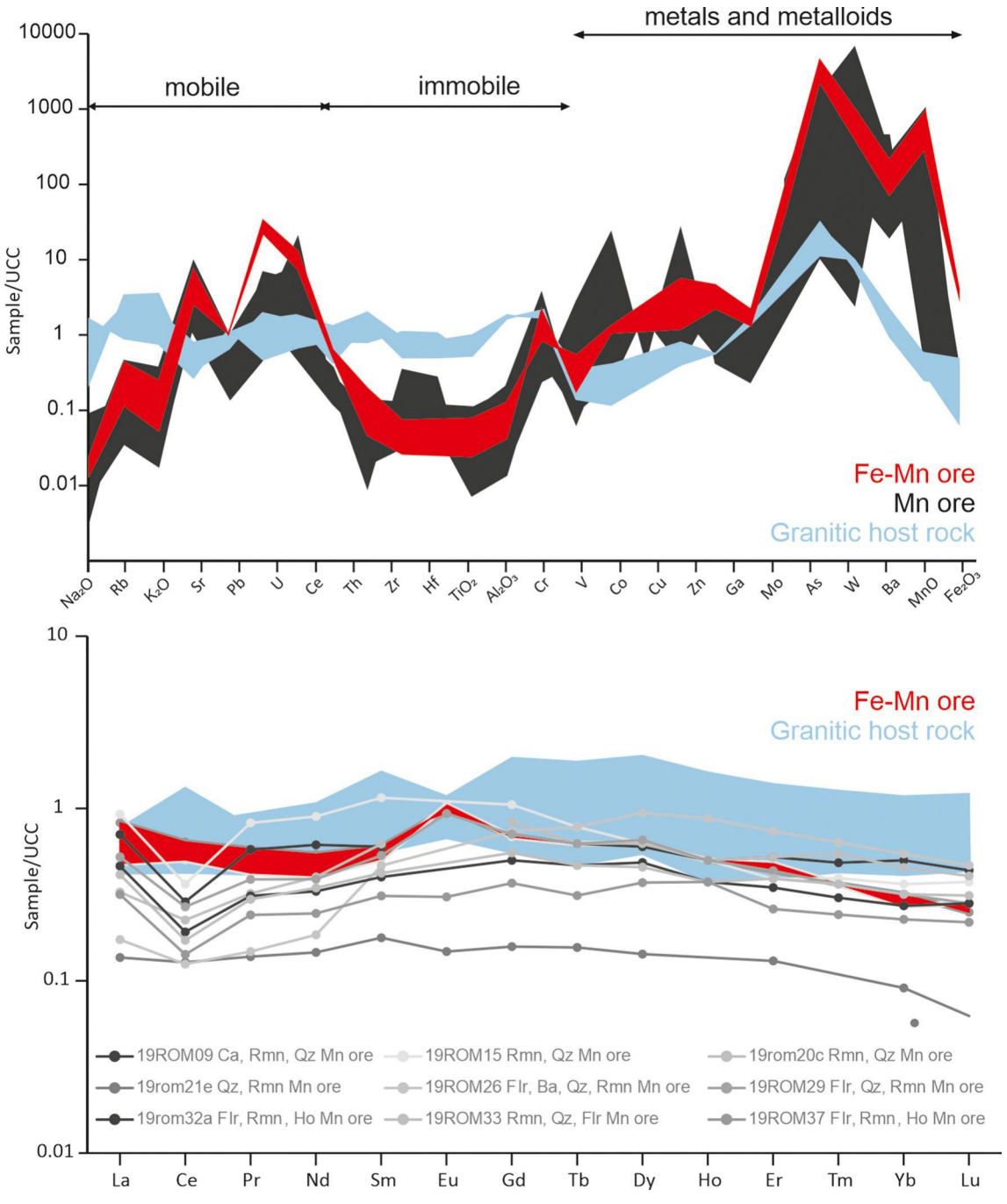
metals and metalloids
mobile
immobile
10000
1000
100
10
1
0.1
0.01
Sample/UCC
Fe-Mn ore
Mn ore
Granitic host rock
Na2O
Rb
K2O
Sr
Pb
U
Ce
Th
Zr
Hf
TiO2
Al2O3
Cr
V
Co
Cu
Zn
Ga
Mo
As
W
Ba
MnO
Fe2O3
10
1
0.1
0.01
Sample/UCC
Fe-Mn ore
Granitic host rock
19ROM09 Ca, Rmn, Qz Mn ore
19ROM15 Rmn, Qz Mn ore
19rom20c Rmn, Qz Mn ore
19rom21e Qz, Rmn Mn ore
19ROM26 Flr, Ba, Qz, Rmn Mn ore
19ROM29 Flr, Qz, Rmn Mn ore
19rom32a Flr, Rmn, Ho Mn ore
19ROM33 Rmn, Qz, Flr Mn ore
19ROM37 Flr, Rmn, Ho Mn ore
La
Ce
Pr
Nd
Sm
Eu
Gd
Tb
Dy
Ho
Er
Tm
Yb
Lu

Figure 5

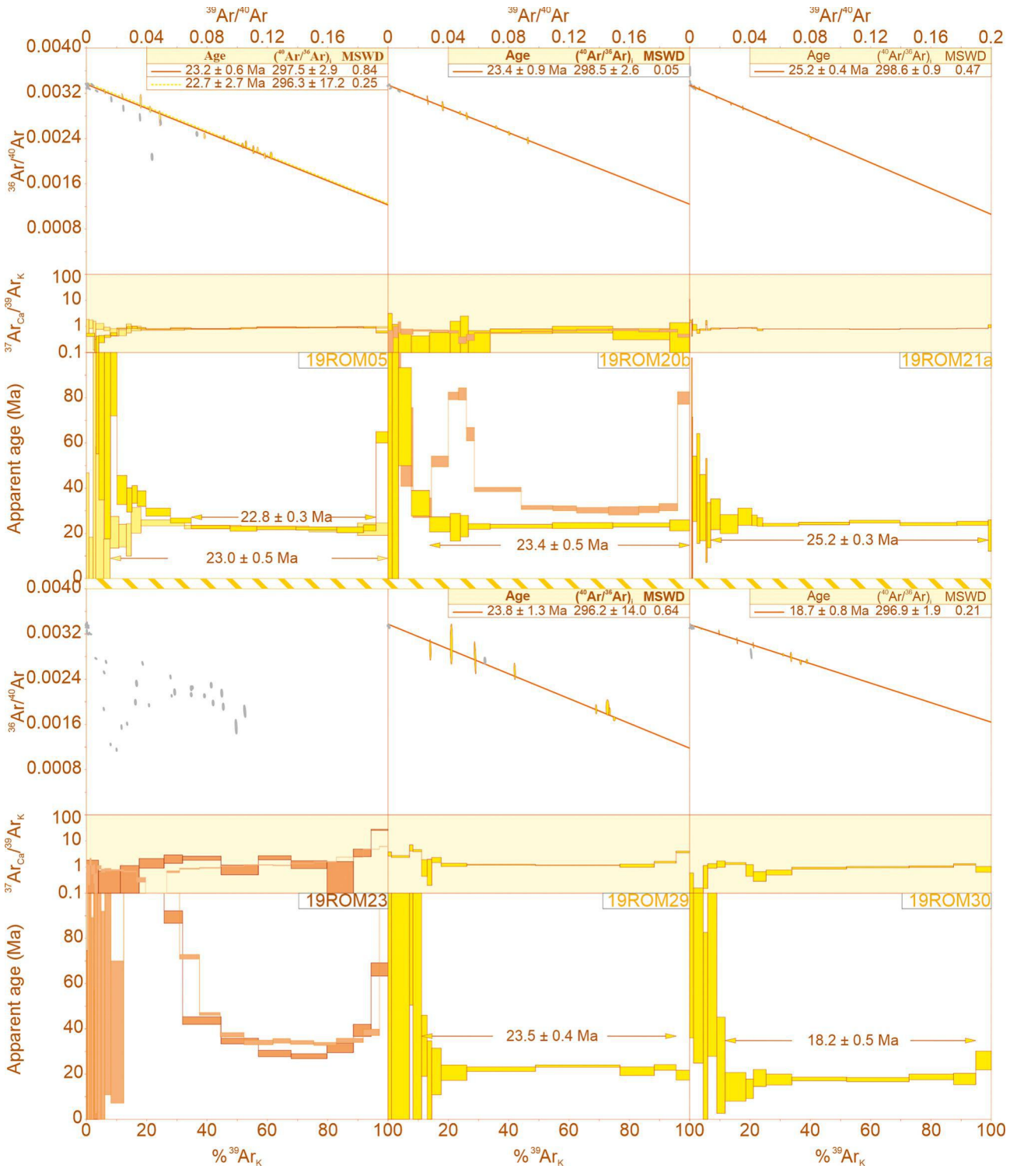
39Ar/40Ar
36Ar/40Ar
37ArCa/39ArK
Apparent age (Ma)
%39ArK
Age (40Ar/36Ar)i MSWD
23.2 ± 0.6 Ma 297.5 ± 2.9 0.84
22.7 ± 2.7 Ma 296.3 ± 17.2 0.25
23.4 ± 0.9 Ma 298.5 ± 2.6 0.05
25.2 ± 0.4 Ma 298.6 ± 0.9 0.47
23.8 ± 1.3 Ma 296.2 ± 14.0 0.64
18.7 ± 0.8 Ma 296.9 ± 1.9 0.21
19ROM05
19ROM20b
19ROM21a
19ROM23
19ROM29
19ROM30
22.8 ± 0.3 Ma
23.0 ± 0.5 Ma
23.4 ± 0.5 Ma
25.2 ± 0.3 Ma
23.5 ± 0.4 Ma
18.2 ± 0.5 Ma

Figure 6

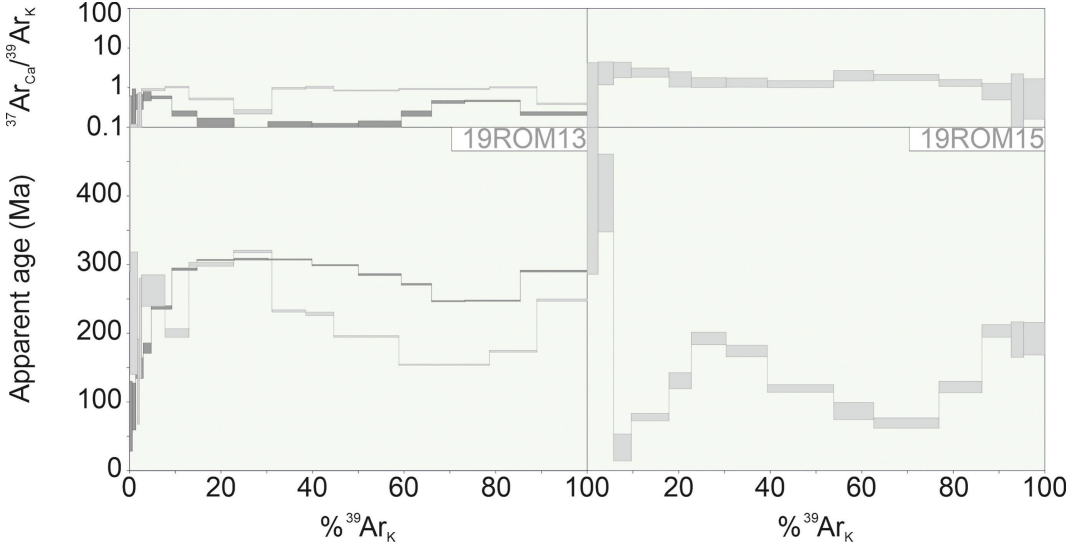
$^{37}Ar_{Ca}/^{39}Ar_K$
100
10
1
0.1
19ROM13
19ROM15
Apparent age (Ma)
400
300
200
100
0
0
20
40
60
80
100
20
40
60
80
100
% $^{39}Ar_K$
% $^{39}Ar_K$

Figure 7

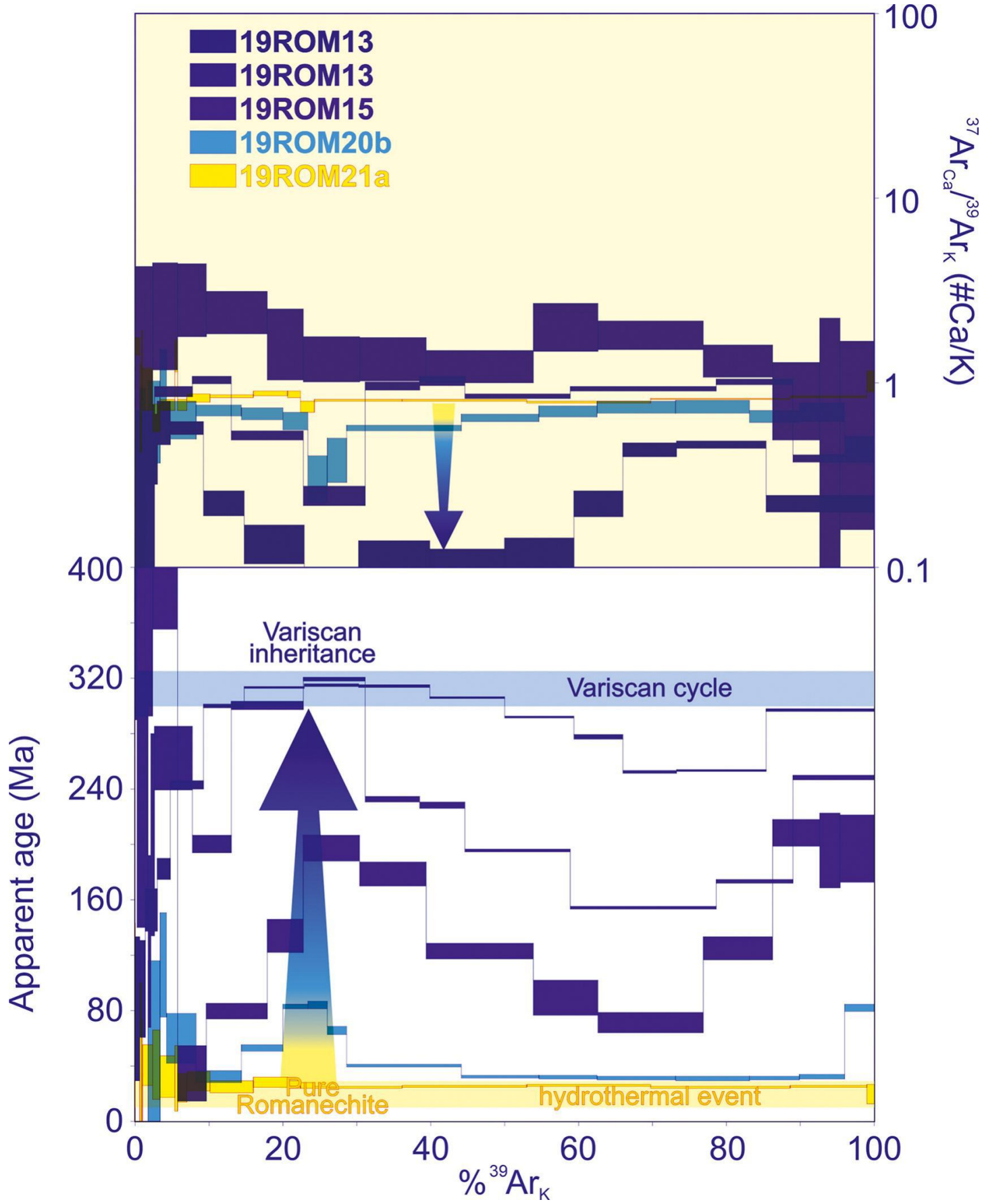
19ROM13
19ROM13
19ROM15
19ROM20b
19ROM21a
100
10
1
0.1
$^{37}Ar_{Ca}/^{39}Ar_K$ (#Ca/K)
400
320
240
160
80
0
Apparent age (Ma)
Variscan inheritance
Variscan cycle
Pure Romanechite
hydrothermal event
0
20
40
60
80
100
% $^{39}Ar_K$

Figure 8

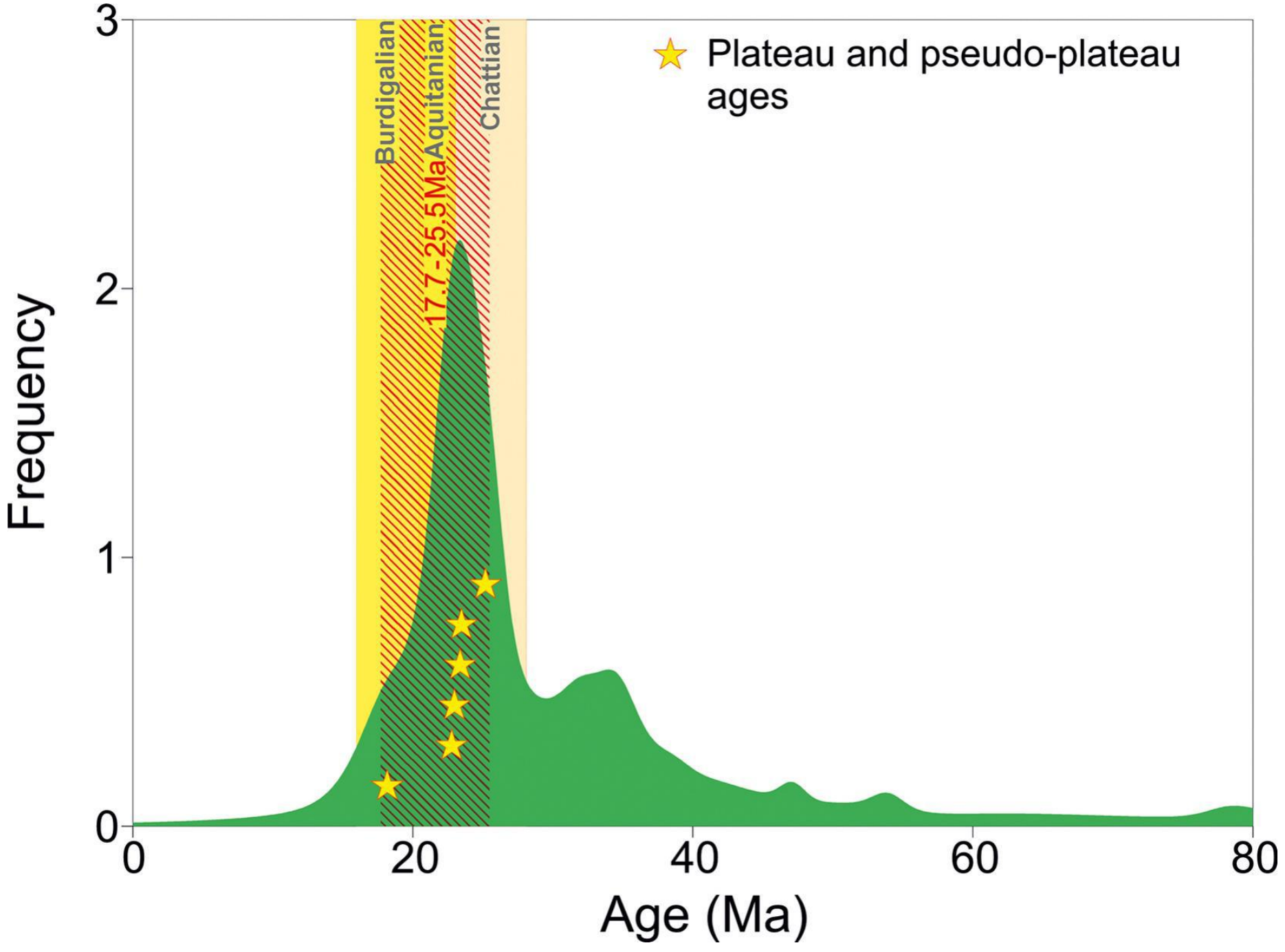
Plateau and pseudo-plateau ages
Burdigalian
Aquitanian
Chattian
17.7-25.5Ma
Frequency
Age (Ma)
0
1
2
3
0
20
40
60
80

Figure 9

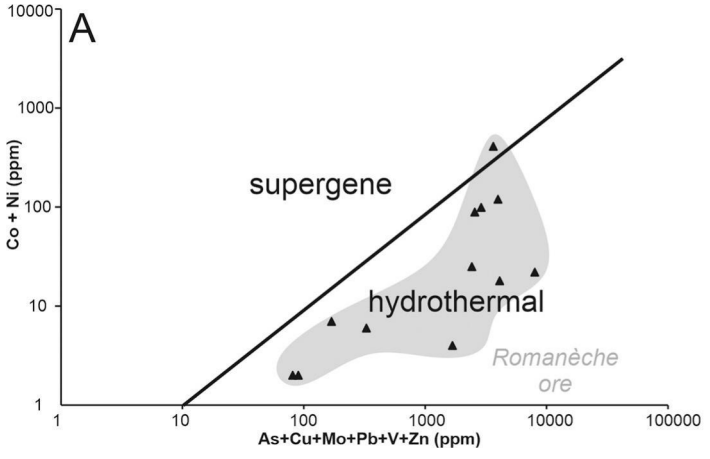
A
supergene
hydrothermal
Romanèche
ore
Co + Ni (ppm)
As+Cu+Mo+Pb+V+Zn (ppm)
10000
1000
100
10
1
1
10
100
1000
10000
100000

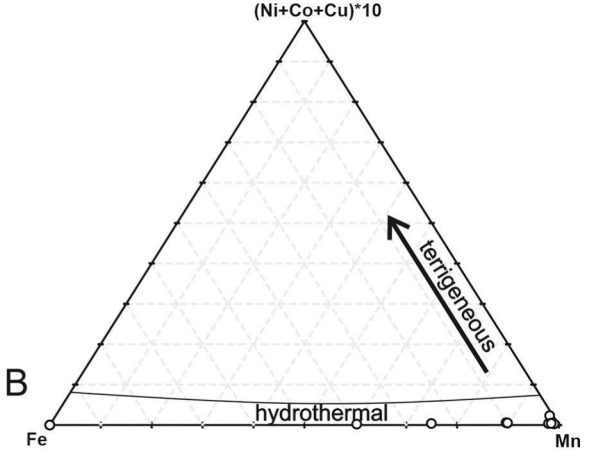
B
(Ni+Co+Cu)*10
terrigeneous
hydrothermal
Fe
Mn

Figure 10